Dynamical evolution of the Uranian satellite system

II. Crossing of the 5/3 Ariel–Umbriel mean motion resonance

Sérgio R. A. Gomes[a,*], Alexandre C. M. Correia[a,b]

[a] CFisUC, Departamento de Física, Universidade de Coimbra, 3004-516 Coimbra, Portugal
[b] IMCCE, UMR8028 CNRS, Observatoire de Paris, PSL Université, 77 Av. Denfert-Rochereau, 75014 Paris, France

ARTICLE INFO

Keywords:
Orbital resonances
Tides
Uranian satellites
Uranus
Natural satellite dynamics

ABSTRACT

At present, the main satellites of Uranus are not involved in any low order mean motion resonance (MMR). However, owing to tides raised in the planet, Ariel and Umbriel most likely crossed the 5/3 MMR in the past. Previous studies on this resonance passage relied on limited time-consuming $N-$body simulations or simplified models focusing solely on the effects of the eccentricity or the inclination. In this paper, we aim to provide a more comprehensive view on how the system evaded capture in the 5/3 MMR. For that purpose, we developed a secular resonant two-satellite model with low eccentricities and low inclinations, including tides using the weak friction model. By performing a large number of numerical simulations, we show that capture in the 5/3 MMR is certain if the initial eccentricities of Ariel, e_1, and Umbriel, e_2, are related through $(e_1^2 + e_2^2)^{1/2} < 0.007$. Moreover, we observe that the eccentricity of Ariel is the key variable to evade the 5/3 MMR with a high probability. We determine that for $e_1 > 0.015$ and $e_2 < 0.01$, the system avoids capture in at least 60% of the cases. We also show that, to replicate the currently observed system, the initial inclinations of Ariel and Umbriel must lay within $I_1 \leq 0.05°$ and $0.06° \leq I_2 \leq 0.11°$, respectively. We checked these results using a complete $N-$body model with the five main satellites and did not observe any significant differences.

1. Introduction

The Uranian satellite system is very intricate, with a rich dynamical and geological past. Results from the only spacecraft that visited this remote planet, Voyager 2, have shown that, among the five regular moons, Miranda, Ariel, and Titania display signs of resurfacing, while Umbriel and Oberon present very cratered ancient surfaces (Smith et al., 1986; Plescia, 1987; Avramchuk et al., 2007). Neither radiogenic nor primordial heat from the formation can solely explain the geological features observed in Miranda, Ariel, and Titania (eg. Peale, 1988; Castillo-Rogez et al., 2023). Since the formation of the Solar System, 4.5 Gyr ago, tidal friction is though to induce a slow outward migration of the satellites (eg. Peale, 1988). The different radial distances of the moons with respect to the planet translate into distinct migration paces, changing the relative distance between the satellites. This probably led to several mean motion resonances (MMRs) encounters (eg. Greenberg, 1975; Smith et al., 1986; Strom, 1987; Peale, 1988). Such events are often invoked as an energy source to explain the features observed on the satellites' surfaces.

The currently observed eccentricities of the Uranian satellites are small, but still abnormally high when tidal dissipation is taken into account. Indeed, tides are expected to damp the free eccentricity on a $10^7 - 10^8$ timescale (Squyres et al., 1985; Gomes and Correia, 2024a), and the forced eccentricity oscillations owing to mutual perturbations between the satellites cannot explain the present values (Dermott and Nicholson, 1986; Laskar, 1986; Gomes and Correia, 2024a). Furthermore, the current inclination of Miranda, $\sim 4.3°$, is also notably high (Tittemore and Wisdom, 1989, 1990; Malhotra and Dermott, 1990; Verheylewegen et al., 2013; Ćuk et al., 2020). The origin of the Uranian satellite system is not yet completely understood, and it is still under debate, but the main satellites likely formed in a circumplanetary disk (eg. Pollack et al., 1991; Szulágyi et al., 2018; Ishizawa et al., 2019; Inderbitzi et al., 2020; Ida et al., 2020; Rufu and Canup, 2022). Regardless of the formation mechanism, the initial eccentricities and inclinations of the main satellites should have been extremely small. The relatively high eccentricities of the satellites and the inclination of Miranda are then clear indicators of a dynamically rich past, were MMR may have played a preponderant role.

sergio.ra.gomes@outlook.com (S.R.A. Gomes); acor@uc.pt (A.C.M. Correia)
ORCID(s):

At present, there is no resonant commensurabilities within the Uranian system (Gomes and Correia, 2024a). As a result, we can infer that the system always managed to escape previous encounters with some MMR. Adopting similar dissipation rates for all satellites, the last commensurability to have been experienced was presumably the 5/3 MMR between Ariel and Umbriel (Peale, 1988; Ćuk et al., 2020; Gomes and Correia, 2023, 2024a). This event is reinforced by the younger predicted ages of Ariel's geological features (eg. Zahnle et al., 2003; Cartwright et al., 2020).

Previous studies were conducted to study the passage of Ariel and Umbriel through the 5/3 MMR. Using a resonant two-satellite planar model with small eccentricities, Tittemore and Wisdom (1988) concluded that if the resonance is approached with eccentricities of both satellites smaller than ~ 0.01, then capture is certain. These eccentricity values are higher than the presently observed ones, and so it remains difficult to explain how the satellites may have acquired such an eccentricity prior to the resonance encounter, such that they can avoid capture.

Ćuk et al. (2020) also studied the passage through the 5/3 MMR, but using a $N-$body numerical integrator, which included the five regular satellites with non-planar, eccentric orbits and spin evolution. Starting with the current eccentricities and nearly zero inclinations, they confirm that Ariel and Umbriel are captured in resonance, as predicted by Tittemore and Wisdom (1988), but posteriorly evaded it due to the chaotic excitation of the eccentricities and inclinations. These chaotic variations are not limited to the two satellites involved in the 5/3 MMR, they also propagate to the orbits of the remaining three satellites. This outcome is particularly significant for the inclination of Miranda: it can attain value higher than 5°, which is comparable to the presently observed value. However, the inclinations of the remaining satellites also grow to values around 1°, which cannot be conciliated with the presently observed low values. Indeed, contrarily to the eccentricities, tides are not very efficient to damp the inclinations, and so their values are presumably fossilised after the resonance crossing. Ćuk et al. (2020) additionally show that a spin-orbit resonance between Umbriel's node and the spin of Oberon can decrease Umbriel's inclination, but this spin-orbit resonance is not observed today and this mechanism also fails to damp the inclinations of the remaining satellites (Gomes and Correia, 2024a).

To better understand the impact of the inclination on the passage of the 5/3 MMR, Gomes and Correia (2023) revisited this problem both analytically and numerically, using a secular two-satellite circular model with small inclinations. Despite the chaotic behaviour, it was shown that a non-zero inclination of Umbriel also facilitates the crossing of this resonance. Moreover, the currently observed inclinations were used to constrain the initial configuration of the system before the resonant encounter. However, in a non-circular model, the eccentricity terms introduce more resonant angles into the problem, that result in additional libration and chaotic regions (Tittemore and Wisdom, 1988). Indeed, for the 3/1 MMR between Miranda and Umbriel, it was shown that the coupling between the eccentricity and inclination resonances may cause significant variations in the eccentricity evolution of Miranda (Tittemore and Wisdom, 1990). Finally, the presence of the remaining three large satellites or Uranus can also introduce three-body resonances that may further excite the eccentricities and the inclinations (Ćuk et al., 2020).

In this paper we aim to understand how the Uranian system evaded the 5/3 MMR between Ariel and Umbriel. To this end, in Sect. 2, we extend the model presented in Gomes and Correia (2023) by developing a secular two-satellite model with small eccentricities and small inclinations. In Sect. 3, we add the tidal effects to the equations of motion using a constant time-lag model. In Sect. 4, we analyse in detail the planar dynamics, which is a simpler two degree-of-freedom problem. This allows us to compare with previous studies (Tittemore and Wisdom, 1988) and better understand the outcomes of the full problem. In Sect. 5, we consider the complete secular problem and perform a large number of numerical simulations to estimate the possible outcomes of the crossing of the 5/3 MMR. In Sect. 6, we compare the secular model with the results of $N-$body simulations, which include the five main satellites. Finally, in the last section, we summarise and discuss our results. In a companion paper (Gomes and Correia, 2024a), hereafter Paper I, we explore the subsequent evolution of the system after the crossing of the 5/3 MMR until the present day.

2. Secular resonant model

In this section, we extend the model presented in Gomes and Correia (2023) by developing a secular two-satellite model for a system involved in a second order $(p+q)/p$ MMR (hence $q=2$) with small eccentricities and small inclinations. We have $p=3$ for the 5/3 MMR, but our model is still valid for any p value.

We consider an oblate central body of mass m_0 (Uranus) surrounded by two point-mass bodies m_1, $m_2 \ll m_0$ (satellites), where the subscript 1 refers to the inner orbit (Ariel) and the subscript 2 refers to the outer orbit (Umbriel).

Table 1
Physical and mean orbital parameters of the five largest Uranian satellites. The masses and orbital parameters are from Jacobson (2014), the radius from Thomas (1988), the second order gravity field, J_2, and the tidal Love numbers are from Table 2 in Chen et al. (2014). The fluid potential Love number, k_f, and the inner structure coefficient, ζ, are from Gomes and Correia (2024a).

	Uranus	Miranda	Ariel	Umbriel	Titania	Oberon
Mass ($\times 10^{-10}\,M_\odot$)	$4.365\,628\times10^{5}$	0.323997	6.291561	6.412118	17.096471	15.468953
Radius (km)	25 559	235.8	578.9	584.7	788.4	761.2
J_2	3.5107×10^{-3}	6.10×10^{-3}	1.39×10^{-3}	6.13×10^{-4}	1.13×10^{-4}	1.48×10^{-5}
ζ	0.225	0.327	0.320	0.342	0.326	0.310
k_f	0.356	0.907	0.862	1.016	0.899	0.790
k_2	0.104	8.84×10^{-4}	1.02×10^{-3}	7.35×10^{-3}	1.99×10^{-2}	1.68×10^{-2}
Period (day)	0.718328	1.413480	2.520381	4.144176	8.705883	13.463254
$a\,(R_0)$		5.080715	7.470167	10.406589	17.069604	22.827536
$e\,(\times10^{-3})$		1.35	1.22	3.94	1.23	1.40
$I\,(^\circ)$		4.4072	0.0167	0.0796	0.1129	0.1478

The potential energy of the system is given by (eg. Smart, 1953)

$$U=-\sum_{k=1}^{2}\frac{\mathcal{G}m_0m_k}{r_k}\left[1+J_2\left(\frac{R_0}{r_k}\right)^2P_2(\hat{\mathbf{r}}_k\cdot\mathbf{s})\right]-\frac{\mathcal{G}m_1m_2}{|\mathbf{r}_2-\mathbf{r}_1|}\,, \tag{1}$$

where $\mathcal{G}$ is the gravitational constant, J_2, R_0 and $\mathbf{s}$ are the second order gravity field, the radius, and the spin unit vector of the central body, respectively, $\mathbf{r}_k$ is the position vector of m_k with respect to the centre-of-mass of m_0 (astrocentric coordinates), $r_k=|\mathbf{r}_k|$ is the norm, $\hat{\mathbf{r}}_k=\mathbf{r}_k/r_k$ is the unit vector, and $P_2(x)=(3x^2-1)/2$ is the Legendre polynomial of degree two. We neglect terms in $(R_0/r_k)^3$ (quadrupolar approximation for the oblateness).

The second order gravity field J_2 mainly depends on Uranus' rotational flattening, and thus on its rotation rate, ω_0. We have (eg. Correia and Rodríguez, 2013)

$$J_2=k_{f,0}\frac{\omega_0^2R_0^3}{3\mathcal{G}m_0}\,, \tag{2}$$

where $k_{f,0}$ is the fluid second Love number for potential. Using the currently observed J_2 and rotation rate of Uranus (Table 1), we compute $k_{f,0}=0.356$.

2.1. Expansion in elliptical elements

The Hamiltonian of the problem, $\mathcal{H}$, is obtained by adding the orbital and rotational kinetic energies to Eq. (1). We can then expand the Hamiltonian in elliptical elements. To the first order in the mass ratios, m_k/m_0, and second order in the eccentricities, e_k, and the inclinations, I_k (with respect to the equatorial plane of the central body), we have (eg. Murray and Dermott, 2000)

$$\mathcal{H}=\mathcal{H}_K+\mathcal{H}_O+\mathcal{H}_S+\mathcal{H}_R+\mathcal{H}_F+\mathcal{H}_\Theta\,, \tag{3}$$

where

$$\mathcal{H}_K=-\sum_{k=1}^{2}\frac{\mathcal{G}m_0m_k}{2a_k} \tag{4}$$

is the Keplerian part and a_k are the semi-major axes,

$$\begin{aligned}\mathcal{H}_O = -\sum_{k=1}^{2} \frac{\mathcal{G}m_0 m_k}{2a_k} J_2 \left(\frac{R_0}{a_k}\right)^2 \Bigg[& 1 + 3e_k \cos\left(\lambda_k - \varpi_k\right) \\ & + \frac{3}{2} e_k^2 \Big(1 + 3\cos\left(2\lambda_k - 2\varpi_k\right)\Big) \\ & - \frac{3}{2} I_k^2 \Big(1 - \cos\left(2\lambda_k - 2\Omega_k\right)\Big) \Bigg]\end{aligned} \tag{5}$$

is the contribution from the oblateness of the planet, λ_k are the mean longitudes, ϖ_k are the longitudes of the pericentre, and Ω_k are the longitudes of the nodes,

$$\begin{aligned}\mathcal{H}_S = -\frac{\mathcal{G}m_1 m_2}{8a_2} \Bigg[& 4b_{1/2}^{(0)}(\alpha) + \left(e_1^2 + e_2^2\right)\left(2\alpha\mathcal{D} + \alpha^2\mathcal{D}^2\right) b_{1/2}^{(0)}(\alpha) \\ & + 2e_1 e_2 \cos\left(\varpi_2 - \varpi_1\right)\left(2 - 2\alpha - \alpha^2\right) b_{1/2}^{(1)}(\alpha) \\ & - \left(I_1^2 + I_2^2 - 2I_1 I_2 \cos\left(\Omega_2 - \Omega_1\right)\right) \alpha\, b_{3/2}^{(1)}(\alpha) \Bigg]\end{aligned} \tag{6}$$

is the secular part, $b_s^{(j)}$ are Laplace coefficients, $\alpha = a_1/a_2$ is the semi-major axes ratio, $\mathcal{D} = \frac{\partial}{\partial\alpha}$, and

$$\begin{aligned}\mathcal{H}_R = -\frac{\mathcal{G}m_1 m_2}{8a_2} \Bigg[& e_1^2 \left(4p^2 + 11p + 6 + (4p+6)\alpha\mathcal{D} + \alpha^2\mathcal{D}^2\right) b_{1/2}^{(p+2)}(\alpha) \\ & \times \cos\left((p+2)\lambda_2 - p\lambda_1 - 2\varpi_1\right) \\ & - e_2^2 \left(27\alpha + 3\alpha^{-2}\right) \cos\left(3\lambda_2 - \lambda_1 - 2\varpi_2\right) \\ & + e_2^2 \left(4p^2 + 9p + 4 + (4p+6)\alpha\mathcal{D} + \alpha^2\mathcal{D}^2\right) b_{1/2}^{(p)}(\alpha) \\ & \times \cos\left((p+2)\lambda_2 - p\lambda_1 - 2\varpi_2\right) \\ & - 2e_1 e_2 \left(4p^2 + 10p + 6 + (4p+6)\alpha\mathcal{D} + \alpha^2\mathcal{D}^2\right) b_{1/2}^{(p+1)}(\alpha) \\ & \times \cos\left((p+2)\lambda_2 - p\lambda_1 - \varpi_1 - \varpi_2\right) \\ & + I_1^2\, \alpha b_{3/2}^{(p+1)}(\alpha) \cos\left((p+2)\lambda_2 - p\lambda_1 - 2\Omega_1\right) \\ & + I_2^2\, \alpha b_{3/2}^{(p+1)}(\alpha) \cos\left((p+2)\lambda_2 - p\lambda_1 - 2\Omega_2\right) \\ & - 2I_1 I_2\, \alpha b_{3/2}^{(p+1)}(\alpha) \cos\left((p+2)\lambda_2 - p\lambda_1 - \Omega_2 - \Omega_1\right) \Bigg],\end{aligned} \tag{7}$$

is the contribution from the second order resonant terms ($q = 2$). The term in $\mathcal{H}_F$ corresponds to the remaining terms of the disturbing function that depend on other combinations of the angles λ_1, λ_2, ϖ_1, ϖ_2, Ω_1, and Ω_2 that do not appear in the expressions of $\mathcal{H}_S$ or $\mathcal{H}_R$. Finally, the last term in the Hamiltonian (Eq. (3)), corresponds to the total rotational kinetic energy. We assume that all bodies rotate about the axis of maximal inertia (gyroscopic approximation), and thus (eg. Goldstein, 1950)

$$\mathcal{H}_\Theta = \sum_{k=0}^{2} \frac{\Theta_k^2}{2C_k}\,, \tag{8}$$

where $C_k = \zeta_k m_k R_k^2$ is the principal moment of inertia, ζ_k is a structure constant (Table 1),

$$\Theta_k = C_k\, \omega_k \tag{9}$$

is the rotational angular momentum, $\omega_k = \dot{\theta}_k$ is the rotational angular velocity, and θ_k is the rotation angle.

2.2. Action-angle resonant variables

We can rewrite the Hamiltonian (Eq. (3)) using a set of canonical action-angle variables. For that purpose, we adopt Andoyer variables for the rotation (Θ_k, θ_k), and Poincaré variables for the orbits $(\Lambda_k, \lambda_k; \Sigma_k, -\varpi_k; \Phi_k, -\Omega_k)$, with

$$\Lambda_k = \beta_k \sqrt{\mu_k a_k} \,, \tag{10}$$

$$\Sigma_k = \Lambda_k \left(1 - \sqrt{1 - e_k^2} \right) \approx \frac{1}{2} \Lambda_k e_k^2 \,, \tag{11}$$

$$\Phi_k = \left(\Lambda_k - \Sigma_k \right) \left(1 - \cos I_k \right) \approx \frac{1}{2} \Lambda_k I_k^2 \,, \tag{12}$$

where $\beta_k = m_0 m_k / (m_0 + m_k)$ and $\mu_k = \mathcal{G}(m_0 + m_k)$. Since we aim to study the dynamics of the system near the $(p+2)/p$ MMR, we introduce the near resonant angle

$$\sigma = \left(1 + \frac{p}{2} \right) \lambda_2 - \frac{p}{2} \lambda_1 \,, \tag{13}$$

which is present in all terms of the resonant Hamiltonian (Eq. (7)). Each term corresponds to a resonant combination:

$$\begin{aligned} &\sigma_1 = \sigma - \varpi_1 \,, \quad \sigma_2 = \sigma - \varpi_2 \,, \quad \sigma_3 = (\sigma_1 + \sigma_2)/2 \,, \\ &\varphi_1 = \sigma - \Omega_1 \,, \quad \varphi_2 = \sigma - \Omega_2 \,, \quad \varphi_3 = (\varphi_1 + \varphi_2)/2 \,. \end{aligned} \tag{14}$$

We additionally introduce the angle

$$\gamma = \frac{p}{2} \left(\lambda_1 - \lambda_2 \right) = \lambda_2 - \sigma \,, \tag{15}$$

and modify the rotation variables as

$$\vartheta_0 = \theta_0 - \sigma \,, \quad \vartheta_1 = \theta_1 - \sigma \quad \text{and} \quad \vartheta_2 = \theta_2 - \sigma \,, \tag{16}$$

such that

$$\begin{bmatrix} \sigma \\ \gamma \\ \sigma_1 \\ \sigma_2 \\ \varphi_1 \\ \varphi_2 \\ \vartheta_0 \\ \vartheta_1 \\ \vartheta_2 \end{bmatrix} \equiv \mathcal{S} \begin{bmatrix} \lambda_1 \\ \lambda_2 \\ -\varpi_1 \\ -\varpi_2 \\ -\Omega_1 \\ -\Omega_2 \\ \theta_0 \\ \theta_1 \\ \theta_2 \end{bmatrix} , \tag{17}$$

with

$$\mathcal{S} = \begin{bmatrix} -p/2 & 1+p/2 & 0 & 0 & 0 & 0 & 0 & 0 & 0 \\ p/2 & -p/2 & 0 & 0 & 0 & 0 & 0 & 0 & 0 \\ -p/2 & 1+p/2 & 1 & 0 & 0 & 0 & 0 & 0 & 0 \\ -p/2 & 1+p/2 & 0 & 1 & 0 & 0 & 0 & 0 & 0 \\ -p/2 & 1+p/2 & 0 & 0 & 1 & 0 & 0 & 0 & 0 \\ -p/2 & 1+p/2 & 0 & 0 & 0 & 1 & 0 & 0 & 0 \\ p/2 & -1-p/2 & 0 & 0 & 0 & 0 & 1 & 0 & 0 \\ p/2 & -1-p/2 & 0 & 0 & 0 & 0 & 0 & 1 & 0 \\ p/2 & -1-p/2 & 0 & 0 & 0 & 0 & 0 & 0 & 1 \end{bmatrix} . \tag{18}$$

We then obtain for the canonical conjugated actions (eg., Goldstein, 1950)

$$\begin{bmatrix} \Sigma \\ \Gamma \\ \tilde{\Sigma}_1 \\ \tilde{\Sigma}_2 \\ \tilde{\Phi}_1 \\ \tilde{\Phi}_2 \\ \tilde{\Theta}_0 \\ \tilde{\Theta}_1 \\ \tilde{\Theta}_2 \end{bmatrix} = (S^{-1})^T \begin{bmatrix} \Lambda_1 \\ \Lambda_2 \\ \Sigma_1 \\ \Sigma_2 \\ \Phi_1 \\ \Phi_2 \\ \Theta_0 \\ \Theta_1 \\ \Theta_2 \end{bmatrix} , \tag{19}$$

where

$$\Sigma = \Lambda_1 + \Lambda_2 - \Sigma_1 - \Sigma_2 - \Phi_1 - \Phi_2 + \Theta_0 + \Theta_1 + \Theta_2 \, , \tag{20}$$

$$\Gamma = \left(1 + \frac{2}{p}\right) \Lambda_1 + \Lambda_2 \, , \tag{21}$$

$$\tilde{\Sigma}_k = \Sigma_k \, , \quad \tilde{\Phi}_k = \Phi_k \, , \quad \text{and} \quad \tilde{\Theta}_k = \Theta_k \, . \tag{22}$$

2.2.1. Conserved quantities

We can rewrite the Hamiltonian (Eq. (3)) using the resonant canonical variables (Eq. (19)). For the actions, we can replace the semi-major axes, the eccentricities, and the inclinations using the relations (10), (11) and (12). We obtain

$$a_k = \frac{\Lambda_k^2}{\beta_k^2 \mu_k} \, , \quad e_k \approx \sqrt{\frac{2\Sigma_k}{\Lambda_k}} \, , \quad \text{and} \quad I_k \approx \sqrt{\frac{2\Phi_k}{\Lambda_k}} \, . \tag{23}$$

Since Λ_k are no longer actions of the resonant variables, they must be obtained from the canonical actions (Eq. (19)) as

$$\Lambda_1 = \Gamma_1 - \frac{p}{2}(\Sigma_1 + \Sigma_2 + \Phi_1 + \Phi_2) \, , \tag{24}$$

$$\Lambda_2 = \Gamma_2 + \left(1 + \frac{p}{2}\right)(\Sigma_1 + \Sigma_2 + \Phi_1 + \Phi_2) \, , \tag{25}$$

where

$$\Gamma_1 = \frac{p}{2}\Gamma(1 - \Delta) \quad \text{and} \quad \Gamma_2 = -\frac{p}{2}\Gamma\left(1 - \left(1 + \frac{2}{p}\right)\Delta\right) \, , \tag{26}$$

with

$$\Delta = (\Sigma - \Theta)/\Gamma \quad \text{and} \quad \Theta = \Theta_0 + \Theta_1 + \Theta_2 \, . \tag{27}$$

In the approximation of small eccentricities and inclinations, we have $\Sigma_k \ll \Lambda_k$ and $\Phi_k \ll \Lambda_k$ (Eq. (23)), and so we also have $\Sigma_k \ll \Gamma_k$ and $\Phi_k \ll \Gamma_k$, which allows us to write

$$\Lambda_1^\alpha \approx \Gamma_1^\alpha \left[1 - \alpha \, \frac{p}{2} \frac{\Sigma_1 + \Sigma_2 + \Phi_1 + \Phi_2}{\Gamma_1}\right] \, , \tag{28}$$

$$\Lambda_2^\alpha \approx \Gamma_2^\alpha \left[1 + \alpha \, \left(1 + \frac{p}{2}\right) \frac{\Sigma_1 + \Sigma_2 + \Phi_1 + \Phi_2}{\Gamma_2}\right] \, , \tag{29}$$

$$e_k \approx \sqrt{\frac{2\Sigma_k}{\Gamma_k}}\,, \quad \text{and} \quad I_k \approx \sqrt{\frac{2\Phi_k}{\Gamma_k}}\,. \tag{30}$$

The replacement of the resonant angles is straightforward (Eq. (17)). The rotation angles θ_k do not appear in the expression of the Hamiltonian (Eq. (3)). Then, the canonical angles ϑ_k also do not appear, and so their conjugated actions, Θ_k, are constants of motion, and so is Θ (Eq. (27)). The remaining angles are combined as (Eqs. (5)−(7))

$$\cos\left(k_1\lambda_1 + k_2\lambda_2 + k_3\varpi_1 + k_4\varpi_2 + k_5\Omega_1 + k_6\Omega_2\right)\,, \quad k_j \in \mathbb{Z}\,, \tag{31}$$

with $\sum_j k_j = 0$, which corresponds to the d'Alembert rule (conservation of the angular momentum). Then, using the resonant angles (Eq. (17)), we obtain for all terms

$$\cos\left(\left(k_1 + \frac{2}{p}k_1 + k_2\right)\gamma - k_3\sigma_1 - k_4\sigma_2 - k_5\varphi_1 - k_6\varphi_2\right)\,. \tag{32}$$

The angle σ does not appear in the Hamiltonian (Eq. (3)), and so its conjugated action, Σ (Eq. (20)), is also a constant of motion.

2.2.2. Average

Near the MMR, the resonant angles σ_k and φ_k vary much slower than γ, that is, $\dot{\sigma_k}, \dot{\varphi_k} \ll \dot{\gamma}$. Therefore, to the first order in m_k/m_0, we can construct the resonant secular normal form of the Hamiltonian (Eq. (3)) by simply averaging over γ:

$$\bar{\mathcal{H}} = \langle\mathcal{H}\rangle_\gamma = \frac{1}{2p\pi}\int_0^{2p\pi} \mathcal{H}\, d\gamma\,. \tag{33}$$

As a result, $\langle\mathcal{H}_F\rangle_\gamma = 0$, and since γ no longer appears in the expression of the averaged Hamiltonian, the conjugated variable, Γ (Eq. (19)), also becomes a constant of motion. We thus reduce a problem with initially nine degrees-of-freedom to a problem with four degrees-of-freedom, $(\Sigma_1, \sigma_1; \Sigma_2, \sigma_2; \Phi_1, \varphi_1; \Phi_2, \varphi_2)$, and five parameters, Σ, Γ, Θ_0, Θ_1 and Θ_2. The auxiliary quantities Γ_1, Γ_2 (Eq. (26)), and Δ (Eq. (27)) are also constant.

The resonant secular Hamiltonian then finally reads

$$\begin{aligned}
\bar{\mathcal{H}} &= (\mathcal{K}_1 + \mathcal{S}_1)(\Sigma_1 + \Sigma_2 + \Phi_1 + \Phi_2) \\
&+ \mathcal{K}_2(\Sigma_1 + \Sigma_2 + \Phi_1 + \Phi_2)^2 \\
&+ (\mathcal{O}_1 + \mathcal{S}_2)\Sigma_1 + (\mathcal{O}_2 + \mathcal{S}_3)\Sigma_2 \\
&+ \mathcal{S}_4\sqrt{\Sigma_1}\sqrt{\Sigma_2}\cos(\sigma_1 - \sigma_2) \\
&+ (\mathcal{O}_3 + \mathcal{S}_5)\Phi_1 + (\mathcal{O}_4 + \mathcal{S}_6)\Phi_2 \\
&+ \mathcal{S}_7\sqrt{\Phi_1}\sqrt{\Phi_2}\cos(\varphi_1 - \varphi_2) \\
&+ \mathcal{R}_1\Sigma_1\cos(2\sigma_1) + \mathcal{R}_2\Sigma_2\cos(2\sigma_2) \\
&+ \mathcal{R}_3\sqrt{\Sigma_1}\sqrt{\Sigma_2}\cos(\sigma_1 + \sigma_2) \\
&+ \mathcal{R}_4\Phi_1\cos(2\varphi_1) + \mathcal{R}_5\Phi_2\cos(2\varphi_2) \\
&+ \mathcal{R}_6\sqrt{\Phi_1}\sqrt{\Phi_2}\cos(\varphi_1 + \varphi_2)\,,
\end{aligned} \tag{34}$$

where $\mathcal{K}$ stands for the Keplerian coefficients (Eq. (4)), $\mathcal{O}$ for the oblateness coefficients (Eq. (5)), $\mathcal{S}$ for secular coefficients (Eq. (6)) and $\mathcal{R}$ for resonant coefficients (Eq. (7)). The Keplerian part needs to be expanded to the second order in Σ_k and Φ_k (fourth order in the eccentricities and the inclinations) because $\mathcal{K}_2$ is much larger than the remaining coefficients. The explicit expression of all these coefficients is given in Appendix A.

2.3. Complex rectangular coordinates

When expressed in the resonant variables $(\Sigma_k, \sigma_k; \Phi_k, \varphi_k)$, the equations of motion may experience some singularities when $\Sigma_k = 0$ or $\Phi_k = 0$, due to the terms in $\mathcal{S}_4$, $\mathcal{S}_7$, $\mathcal{R}_3$, and $\mathcal{R}_6$ (Eq. (34)). We thus perform a second canonical change of variables to complex rectangular coordinates $(\Sigma_k, \sigma_k; \Phi_k, \varphi_k) \rightarrow (x_k, \mathrm{i}\overline{x}_k; y_k, \mathrm{i}\overline{y}_k)$, where

$$x_k = \sqrt{\Sigma_k}\mathrm{e}^{\mathrm{i}\sigma_k} \quad \text{and} \quad y_k = \sqrt{\Phi_k}\mathrm{e}^{\mathrm{i}\varphi_k} \,, \tag{35}$$

and $\overline{x}_k$ and $\overline{y}_k$ are the complex conjugate of x_k and y_k, respectively. From Eq. (30) we have

$$x_k \approx e_k\sqrt{\frac{\Gamma_k}{2}}\mathrm{e}^{\mathrm{i}\sigma_k} \quad \text{and} \quad y_k \approx I_k\sqrt{\frac{\Gamma_k}{2}}\mathrm{e}^{\mathrm{i}\varphi_k} \,, \tag{36}$$

and so these variables are proportional to the eccentricities and the inclinations, respectively. In this new set of canonical variables, the resonant secular Hamiltonian (Eq. (34)) becomes

$$\begin{aligned}
\bar{\mathcal{H}} &= (\mathcal{K}_1 + \mathcal{S}_1)\left(x_1\overline{x}_1 + x_2\overline{x}_2 + y_1\overline{y}_1 + y_2\overline{y}_2\right) \\
&+ \mathcal{K}_2\left(x_1\overline{x}_1 + x_2\overline{x}_2 + y_1\overline{y}_1 + y_2\overline{y}_2\right)^2 \\
&+ (\mathcal{O}_1 + \mathcal{S}_2)x_1\overline{x}_1 + (\mathcal{O}_2 + \mathcal{S}_3)x_2\overline{x}_2 + \frac{\mathcal{S}_4}{2}\left(x_1\overline{x}_2 + \overline{x}_1x_2\right) \\
&+ (\mathcal{O}_3 + \mathcal{S}_5)y_1\overline{y}_1 + (\mathcal{O}_4 + \mathcal{S}_6)y_2\overline{y}_2 + \frac{\mathcal{S}_7}{2}\left(y_1\overline{y}_2 + \overline{y}_1y_2\right) \\
&+ \frac{\mathcal{R}_1}{2}\left(x_1^2 + \overline{x}_1^2\right) + \frac{\mathcal{R}_2}{2}\left(x_2^2 + \overline{x}_2^2\right) + \frac{\mathcal{R}_3}{2}\left(x_1x_2 + \overline{x}_1\overline{x}_2\right) \\
&+ \frac{\mathcal{R}_4}{2}\left(y_1^2 + \overline{y}_1^2\right) + \frac{\mathcal{R}_5}{2}\left(y_2^2 + \overline{y}_2^2\right) + \frac{\mathcal{R}_6}{2}\left(y_1y_2 + \overline{y}_1\overline{y}_2\right) \,.
\end{aligned} \tag{37}$$

The equations of motion are simply obtained from Eq. (37) using the Hamilton equations, as

$$\dot{x}_k = \mathrm{i}\frac{\partial\bar{\mathcal{H}}}{\partial\overline{x}_k} \quad \text{and} \quad \dot{y}_k = \mathrm{i}\frac{\partial\bar{\mathcal{H}}}{\partial\overline{y}_k} \,, \tag{38}$$

which yields, for the conservative resonant dynamics,

$$\begin{aligned}
\dot{x}_1 = \mathrm{i}\Bigg[&\left(\mathcal{K}_1 + \mathcal{S}_1\right)x_1 + 2\mathcal{K}_2\left(x_1\overline{x}_1 + x_2\overline{x}_2 + y_1\overline{y}_1 + y_2\overline{y}_2\right)x_1 \\
&+ \left(\mathcal{O}_1 + \mathcal{S}_2\right)x_1 + \frac{\mathcal{S}_4}{2}x_2 + \mathcal{R}_1\overline{x}_1 + \frac{\mathcal{R}_3}{2}\overline{x}_2\Bigg] \,,
\end{aligned} \tag{39}$$

$$\begin{aligned}
\dot{x}_2 = \mathrm{i}\Bigg[&\left(\mathcal{K}_1 + \mathcal{S}_1\right)x_2 + 2\mathcal{K}_2\left(x_1\overline{x}_1 + x_2\overline{x}_2 + y_1\overline{y}_1 + y_2\overline{y}_2\right)x_2 \\
&+ \left(\mathcal{O}_2 + \mathcal{S}_3\right)x_2 + \frac{\mathcal{S}_4}{2}x_1 + \mathcal{R}_2\overline{x}_2 + \frac{\mathcal{R}_3}{2}\overline{x}_1\Bigg] \,,
\end{aligned} \tag{40}$$

$$\begin{aligned}
\dot{y}_1 = \mathrm{i}\Bigg[&\left(\mathcal{K}_1 + \mathcal{S}_1\right)y_1 + 2\mathcal{K}_2\left(x_1\overline{x}_1 + x_2\overline{x}_2 + y_1\overline{y}_1 + y_2\overline{y}_2\right)y_1 \\
&+ \left(\mathcal{O}_3 + \mathcal{S}_5\right)y_1 + \frac{\mathcal{S}_7}{2}y_2 + \mathcal{R}_4\overline{y}_1 + \frac{\mathcal{R}_6}{2}\overline{y}_2\Bigg] \,,
\end{aligned} \tag{41}$$

and

$$\dot{y}_2 = \mathrm{i}\left[\left(\mathcal{K}_1 + \mathcal{S}_1\right) y_2 + 2\mathcal{K}_2\left(x_1\bar{x}_1 + x_2\bar{x}_2 + y_1\bar{y}_1 + y_2\bar{y}_2\right) y_2 + \left(\mathcal{O}_4 + \mathcal{S}_6\right) y_2 + \frac{\mathcal{S}_7}{2} y_1 + \mathcal{R}_5\bar{y}_2 + \frac{\mathcal{R}_6}{2}\bar{y}_1\right] . \tag{42}$$

3. Tidal evolution

Up to this point, we only considered the resonant dynamics (Sect. 2), which is conservative and therefore the average semi-major axes remain constant. However, dissipative tidal interactions are expected to induce an orbital evolution of the Uranian satellites. The tidal contributions can be obtained by considering an additional tidal potential (Darwin, 1880; Kaula, 1964; Mignard, 1979).

3.1. Tidal potential energy

Tides arise from differential and inelastic deformations of an extended body owing to the gravitational effect of a perturber. The resulting distortion gives rise to a tidal bulge, which modifies the gravitational potential of the extended body. As the perturber interacts with the additional potential field, the amount of tidal potential energy is given by (eg. Lambeck, 1980)

$$U_{ij} = -k_{2,j}\frac{\mathcal{G}m_i^2}{R_j}\left(\frac{R_j}{r_{ij}}\right)^3\left(\frac{R_j}{r'_{ij}}\right)^3 P_2(\hat{\mathbf{r}}_{ij}\cdot\hat{\mathbf{r}}'_{ij}) , \tag{43}$$

where R_j and $k_{2,j}$ are the radius and the elastic second Love number for potential of the extended body, respectively, and $\mathbf{r}_{ij}$ is the position vector between the centre-of-mass of the extended body and that of the perturber with mass m_i. The tidal friction within the extended body introduces a time delay, τ_j, between the maximal deformation, at $\mathbf{r}_{ij} = \mathbf{r}_{ij}(t)$, and the initial perturbation, at $\mathbf{r}'_{ij} = \mathbf{r}_{ij}(t-\tau_j)$. Although tidal effects do not preserve the total energy, it is possible to extend the Hamiltonian formalism from Sect. 2, by considering the primed quantities, $\mathbf{r}'_{ij}$, as parameters (Mignard, 1979). The tidal Hamiltonian then reads (Eqs. (3) and (43))

$$\mathcal{H}_t = \mathcal{H} + U_{01} + U_{10} + U_{02} + U_{20} . \tag{44}$$

We neglect the satellite-satellite interaction terms, U_{12} and U_{21}. For the considered terms, we note that $\mathbf{r}_{0k} = -\mathbf{r}_{k0} = \mathbf{r}_k$. Therefore, in the following expressions of U_{ij} we assume the subscript $k = \max(i, j)$. As in Sect. 2.1, we first expand U_{ij} in elliptical elements. To the first order in the mass ratios, and second order in the eccentricities and in the inclinations,

we have

$$
\begin{aligned}
U_{ij} = -k_{2,j}\frac{\mathcal{G}m_i^2 R_j^5}{4a_k^3 a_k'^3}\Bigg[& 1 + 3\cos(2\lambda_k - 2\lambda_k' - 2\theta_j + 2\theta_j') \\
& + \frac{3}{2}e_k\Big(2\cos\left(\lambda_k - \varpi_k\right) - \cos\left(\lambda_k - 2\lambda_k' + \varpi_k - 2\theta_j + 2\theta_j'\right) \\
& \qquad + 7\cos\left(3\lambda_k - 2\lambda_k' - \varpi_k - 2\theta_j + 2\theta_j'\right)\Big) \\
& + \frac{3}{2}e_k'\Big(2\cos\left(\lambda_k' - \varpi_k'\right) - \cos\left(2\lambda_k - \lambda_k' - \varpi_k' - 2\theta_j + 2\theta_j'\right) \\
& \qquad + 7\cos\left(2\lambda_k - 3\lambda_k' + \varpi_k' - 2\theta_j + 2\theta_j'\right)\Big) \\
& + \frac{3}{2}e_k^2\Big(1 + 3\cos\left(2\lambda_k - 2\varpi_k\right) \\
& \qquad - 5\cos\left(2\lambda_k - 2\lambda_k' - 2\theta_j + 2\theta_j'\right) \\
& \qquad + 17\cos\left(4\lambda_k - 2\lambda_k' - 2\varpi_k - 2\theta_j + 2\theta_j'\right)\Big) \\
& + \frac{3}{2}e_k'^2\Big(1 + 3\cos\left(2\lambda_k' - 2\varpi_k'\right) \\
& \qquad - 5\cos\left(2\lambda_k - 2\lambda_k' - 2\theta_j + 2\theta_j'\right) \\
& \qquad + 17\cos\left(2\lambda_k - 4\lambda_k' + 2\varpi_k' - 2\theta_j + 2\theta_j'\right)\Big) \\
& + \frac{3}{4}e_k e_k'\Big(6\cos\left(\lambda_k - \lambda_k' - \varpi_k + \varpi_k'\right) \\
& \qquad + 6\cos\left(\lambda_k + \lambda_k' - \varpi_k - \varpi_k'\right) \\
& \qquad + \cos\left(\lambda_l - \lambda_k' + \varpi_k - \varpi_k' - 2\theta_j + 2\theta_j'\right) \\
& \qquad - 9\cos\left(\lambda_l - 3\lambda_k' + \varpi_k + \varpi_k' - 2\theta_j + 2\theta_j'\right) \\
& \qquad - 9\cos\left(3\lambda_l - \lambda_k' - \varpi_k - \varpi_k' - 2\theta_j + 2\theta_j'\right) \\
& \qquad + 47\cos\left(3\lambda_l - 3\lambda_k' - \varpi_k + \varpi_k' - 2\theta_j + 2\theta_j'\right)\Big) \\
& - \frac{3}{2}I_k^2\left(1 - \cos\left(2\lambda_k - 2\Omega_k\right) + \cos\left(2\lambda_k - 2\lambda_k' - 2\theta_j + 2\theta_j'\right) - \cos\left(2\lambda_k' - 2\Omega_k + 2\theta_j - 2\theta_j'\right)\right) \\
& - \frac{3}{2}I_k'^2\left(1 - \cos\left(2\lambda_k' - 2\Omega_k'\right) + \cos\left(2\lambda_k - 2\lambda_k' - 2\theta_j + 2\theta_j'\right) - \cos\left(2\lambda_k - 2\Omega_k' - 2\theta_j + 2\theta_j'\right)\right) \\
& + 3I_k I_k'\Big(\cos\left(2\lambda_k - 2\lambda_k' - \Omega_k + \Omega_k' - \theta_j + \theta_j'\right) + \cos\left(\Omega_k - \Omega_k' - \theta_j + \theta_j'\right) \\
& \qquad - \cos\left(2\lambda_k - \Omega_k - \Omega_k' - \theta_j + \theta_j'\right) \quad - \cos\left(2\lambda_k' - \Omega_k - \Omega_k' + \theta_j - \theta_j'\right)\Big)\Bigg] .
\end{aligned}
\tag{45}
$$

We first perform the canonical change of variables that uses the resonant angles (Eq. (17)) and then change to the complex Cartesian coordinates (Eq. (35)). We get

$$
\begin{aligned}
U_{ij} = -k_{2,j}\frac{\mathcal{G}m_i^2 R_j^5 \beta_k^{12}\mu_k^6}{16\Gamma_k^7\Gamma_k'^7}\Bigg[& 4\Gamma_k\Gamma_k' \\
& + 12\Gamma_k' x_k\bar{x}_k + 12\Gamma_k x_k'\bar{x}_k' - 12\Gamma_k' y_k\bar{y}_k - 12\Gamma_k y_k'\bar{y}_k' \\
& - 24p_k\left(\Gamma_k'(x_1\bar{x}_1 + x_2\bar{x}_2 + y_1\bar{y}_1 + y_2\bar{y}_2\right) \\
& - 24p_k\left(\Gamma_k(x_1'\bar{x}_1' + x_2'\bar{x}_2' + y_1'\bar{y}_1' + y_2'\bar{y}_2'\right) \\
& + 12\Big(\Gamma_k\Gamma_k' - \Gamma_k'(5x_k\bar{x}_k - y_k\bar{y}_k) - \Gamma_k(5x_k'\bar{x}_k' - y_k'\bar{y}_k') \\
& \quad -6p_k\Big(\Gamma_k'(x_1\bar{x}_1 + x_2\bar{x}_2 + y_1\bar{y}_1 + y_2\bar{y}_2) \\
& \quad\quad +\Gamma_k(x_1'\bar{x}_1' + x_2'\bar{x}_2' + y_1'\bar{y}_1' + y_2'\bar{y}_2')\Big)\Big) \\
& \quad\quad \times\cos(2(\vartheta_j - \vartheta_j' - q_k(\gamma - \gamma'))) \\
& + 6\sqrt{2}\,(x_k + \bar{x}_k)\sqrt{\Gamma_k}\Gamma_k'\cos(q_k\gamma) \\
& + 6\sqrt{2}\,(x_k' + \bar{x}_k')\Gamma_k\sqrt{\Gamma_k'}\cos(q_k\gamma') \\
& - 3\sqrt{2}\,(x_k + \bar{x}_k)\sqrt{\Gamma_k}\Gamma_k'\cos\left(q_k(\gamma - 2\gamma') - 2\vartheta_j + 2\vartheta_j'\right) \\
& - 3\sqrt{2}\,(x_k' + \bar{x}_k')\Gamma_k\sqrt{\Gamma_k'}\cos\left(q_k(2\gamma - \gamma') - 2\vartheta_j + 2\vartheta_j'\right) \\
& + 21\sqrt{2}\,(x_k + \bar{x}_k)\sqrt{\Gamma_k}\Gamma_k'\cos\left(q_k(3\gamma - 2\gamma') - 2\vartheta_j + 2\vartheta_j'\right) \\
& + 21\sqrt{2}\,(x_k' + \bar{x}_k')\Gamma_k\sqrt{\Gamma_k'}\cos\left(q_k(2\gamma - 3\gamma') - 2\vartheta_j + 2\vartheta_j'\right) \\
& + 6\Gamma_k\left(3x_k'^2 + 3\bar{x}_k'^2 + y_k'^2 + \bar{y}_k'^2\right)\cos(2q_k\gamma') \\
& + 6\Gamma_k\left(3x_k'^2 + 3\bar{x}_k'^2 + y_k'^2 + \bar{y}_k'^2\right)\cos(2q_k\gamma') \\
& + 18\,\left(x_k\bar{x}_k' + x_k'\bar{x}_k\right)\sqrt{\Gamma_k\Gamma_k'}\cos\left(q_k(\gamma - \gamma')\right) \\
& + 18\,\left(x_k x_k' + \bar{x}_k\bar{x}_k'\right)\sqrt{\Gamma_k\Gamma_k'}\cos\left(q_k(\gamma + \gamma')\right) \\
& + 102\Gamma_k'\left(x_k^2 + \bar{x}_k^2\right)\cos\left(2(2q_k\gamma - q_k\gamma' - \vartheta_j + \vartheta_j')\right) \\
& + 102\Gamma_k\left(x_k'^2 + \bar{x}_k'^2\right)\cos\left(2(q_k\gamma - 2q_k\gamma' - \vartheta_j + \vartheta_j')\right) \\
& + 3\sqrt{\Gamma_k\Gamma_k'}\left(x_k\bar{x}_k' + x_k'\bar{x}_k\right)\cos\left(q_k(\gamma - \gamma') - 2\vartheta_j + 2\vartheta_j'\right) \\
& + 147\sqrt{\Gamma_k\Gamma_k'}\left(x_k\bar{x}_k' + x_k'\bar{x}_k\right)\cos\left(3q_k(\gamma - \gamma') - 2\vartheta_j + 2\vartheta_j'\right) \\
& - 21\sqrt{\Gamma_k\Gamma_k'}\left(x_k x_k' + \bar{x}_k\bar{x}_k'\right)\cos\left(q_k(\gamma - 3\gamma') - 2\vartheta_j + 2\vartheta_j'\right) \\
& - 21\sqrt{\Gamma_k\Gamma_k'}\left(x_k x_k' + \bar{x}_k\bar{x}_k'\right)\cos\left(q_k(3\gamma - \gamma') - 2\vartheta_j + 2\vartheta_j'\right) \\
& + 6\Gamma_k\left(y_k'^2 + \bar{y}_k'^2\right)\cos\left(2(q_k\gamma - \vartheta_j + \vartheta_j')\right) + 6\Gamma_k'\left(y_k^2 + \bar{y}_k^2\right)\cos\left(2(q_k\gamma' + \vartheta_j - \vartheta_j')\right)
\end{aligned}
$$

$$
\begin{aligned}
&+ 12\sqrt{\Gamma_k\Gamma'_k}\left(y_k\overline{y}'_k + y'_k\overline{y}_k\right)\cos\left(\vartheta_j - \vartheta'_j\right)\\
&+ 12\sqrt{\Gamma_k\Gamma'_k}\left(y_k\overline{y}'_k + y'_k\overline{y}_k\right)\cos\left(2q_k(\gamma-\gamma') - \vartheta_j + \vartheta'_j\right)\\
&- 12\sqrt{\Gamma_k\Gamma'_k}\left(y_k y'_k + \overline{y}_k\overline{y}'_k\right)\cos(2q_k\gamma - \vartheta_j + \vartheta'_j)\\
&- 12\sqrt{\Gamma_k\Gamma'_k}\left(y_k y'_k + \overline{y}_k\overline{y}'_k\right)\cos(2q_k\gamma' + \vartheta_j - \vartheta'_j)\\
&+ 6\sqrt{2}\,\mathrm{i}\,(x_k - \overline{x}_k)\sqrt{\Gamma_k}\Gamma'_k\sin(q_k\gamma) + 6\sqrt{2}\,\mathrm{i}\,(x'_k - \overline{x}'_k)\Gamma_k\sqrt{\Gamma'_k}\sin(q_k\gamma')\\
&+ 3\sqrt{2}\,\mathrm{i}\,(x_k - \overline{x}_k)\sqrt{\Gamma_k}\Gamma'_k\sin\left(q_k(\gamma-2\gamma') - 2\vartheta_j + 2\vartheta'_j\right)\\
&- 3\sqrt{2}\,\mathrm{i}\,(x'_k - \overline{x}'_k)\Gamma_k\sqrt{\Gamma'_k}\sin\left(q_k(2\gamma-\gamma') - 2\vartheta_j + 2\vartheta'_j\right)\\
&+ 21\sqrt{2}\,\mathrm{i}\,(x_k - \overline{x}_k)\sqrt{\Gamma_k}\Gamma'_k\sin\left(q_k(3\gamma-2\gamma') - 2\vartheta_j + 2\vartheta'_j\right)\\
&- 21\sqrt{2}\,\mathrm{i}\,(x'_k - \overline{x}'_k)\Gamma_k\sqrt{\Gamma'_k}\sin\left(q_k(2\gamma-3\gamma') - 2\vartheta_j + 2\vartheta'_j\right)\\
&+ 102\,\mathrm{i}\,\Gamma'_k\left(x_k^2 - \overline{x}_k^2\right)\sin\left(2(2q_k\gamma - q_k\gamma' - \vartheta_j + \vartheta'_j)\right)\\
&- 102\,\mathrm{i}\,\Gamma_k\left(x_k'^2 - \overline{x}_k'^2\right)\sin\left(2(q_k\gamma - 2q_k\gamma' - \vartheta_j + \vartheta'_j)\right)\\
&+ 18\,\mathrm{i}\,\left(x_k\overline{x}'_k + x'_k\overline{x}_k\right)\sqrt{\Gamma_k\Gamma'_k}\sin\left(q_k(\gamma-\gamma')\right)\\
&+ 18\,\mathrm{i}\,\left(x_k x'_k + \overline{x}_k\overline{x}'_k\right)\sqrt{\Gamma_k\Gamma'_k}\sin\left(q_k(\gamma+\gamma')\right)\\
&- 3\,\mathrm{i}\,\sqrt{\Gamma_k\Gamma'_k}\left(x_k\overline{x}'_k - x'_k\overline{x}_k\right)\sin\left(q_k(\gamma-\gamma') - 2\vartheta_j + 2\vartheta'_j\right)\\
&+ 147\,\mathrm{i}\,\sqrt{\Gamma_k\Gamma'_k}\left(x_k\overline{x}'_k - x'_k\overline{x}_k\right)\sin\left(3q_k(\gamma-\gamma') - 2\vartheta_j + 2\vartheta'_j\right)\\
&+ 21\,\mathrm{i}\,\sqrt{\Gamma_k\Gamma'_k}\left(x_k x'_k - \overline{x}_k\overline{x}'_k\right)\sin\left(q_k(\gamma-3\gamma') - 2\vartheta_j + 2\vartheta'_j\right)\\
&- 21\,\mathrm{i}\,\sqrt{\Gamma_k\Gamma'_k}\left(x_k x'_k - \overline{x}_k\overline{x}'_k\right)\sin\left(q_k(3\gamma-\gamma') - 2\vartheta_j + 2\vartheta'_j\right)\\
&+ 6\,\mathrm{i}\,\Gamma'_k\left(3x_k^2 - 3\overline{x}_k^2 + y_k^2 - \overline{y}_k^2\right)\sin\left(2q_k\gamma\right)\\
&+ 6\,\mathrm{i}\,\Gamma_k\left(3x_k'^2 - 3\overline{x}_k'^2 + y_k'^2 - \overline{y}_k'^2\right)\sin\left(2q_k\gamma'\right)\\
&+ 6\,\mathrm{i}\,\Gamma'_k\left(y_k^2 - \overline{y}_k^2\right)\sin\left(2(q_k\gamma' + \vartheta_j - \vartheta'_j)\right)\\
&+ 6\,\mathrm{i}\,\Gamma_k\left(y_k'^2 - \overline{y}_k'^2\right)\sin\left(2(q_k\gamma - \vartheta_j + \vartheta'_j)\right)\\
&+ 12\,\mathrm{i}\,\sqrt{\Gamma_k\Gamma'_k}\left(y_k\overline{y}'_k - y'_k\overline{y}_k\right)\sin\left(\vartheta_j - \vartheta'_j\right)\\
&+ 12\,\mathrm{i}\,\sqrt{\Gamma_k\Gamma'_k}\left(y_k\overline{y}'_k - y'_k\overline{y}_k\right)\sin\left(2q_k(\gamma-\gamma') - \vartheta_j + \vartheta'_j\right)\\
&- 12\,\mathrm{i}\,\sqrt{\Gamma_k\Gamma'_k}\left(y_k y'_k - \overline{y}_k\overline{y}'_k\right)\sin(2q_k\gamma - \vartheta_j + \vartheta'_j) - 12\,\mathrm{i}\,\sqrt{\Gamma_k\Gamma'_k}\left(y_k y'_k - \overline{y}_k\overline{y}'_k\right)\sin(2q_k\gamma' + \vartheta_j - \vartheta'_j)\Bigg],
\end{aligned}
\tag{46}
$$

where $p_1 = -p/2$, $p_2 = 1 + p/2$, $q_1 = 1 + 2/p$ and $q_2 = 1$.

We note again that σ does not appear in the expression of U_{ij} (Eq. (46)). As a result, in the presence of tides, the parameter Σ (Eq. (20)) remains conserved. On the other hand, the fast angle γ is still present. Yet, at this stage, we cannot perform an average as in Sect. 2.2.2, because γ' is considered as a parameter that can later cancel with γ (see Eq. (51)).

3.2. Secular equations of motion

The equations of motion are obtained from Eq. (44) using the Hamilton equations. The additional contributions from tides derive only from the U_{ij} (Eq. (46)), and are given by ($k = 1, 2$)

$$\begin{aligned}
\dot{x}_k &= \mathrm{i}\frac{\partial U_{0k}}{\partial \overline{x}_k} + \mathrm{i}\frac{\partial U_{k0}}{\partial \overline{x}_k} \,, \\
\dot{y}_k &= \mathrm{i}\frac{\partial U_{0k}}{\partial \overline{y}_k} + \mathrm{i}\frac{\partial U_{k0}}{\partial \overline{y}_k} \,, \\
\dot{\Theta}_0 &= -\frac{\partial U_{10}}{\partial \vartheta_0} - \frac{\partial U_{20}}{\partial \vartheta_0} \,, \\
\dot{\Theta}_k &= -\frac{\partial U_{0k}}{\partial \vartheta_k} \,, \\
\dot{\Gamma} &= -\frac{\partial U_{01}}{\partial \gamma} - \frac{\partial U_{10}}{\partial \gamma} - \frac{\partial U_{02}}{\partial \gamma} - \frac{\partial U_{20}}{\partial \gamma} \,.
\end{aligned} \tag{47}$$

We should also write the equations for $\dot{\gamma}$ and $\dot{\vartheta}_k$. However, these angles disappear from the equations of motion with some of the following simplifications, and so we do not need them to get a closed set for the secular evolution of the system.

To handle the expression of the primed quantities, we need to use a tidal model. For simplicity, we adopt here the weak friction model (eg. Singer, 1968; Alexander, 1973), which assumes a constant and small time delay between the tidal potential and the perturbing mass, τ_j. This model is widely used and provides simple expressions for the tidal interactions, because it can be made linear (eg. Mignard, 1979),

$$\lambda'_k \approx \lambda_k - n_k \tau_j \,, \quad \text{and} \quad \theta'_j \approx \theta_j - \omega_j \tau_j \,. \tag{48}$$

The remaining primed quantities follow as,

$$x'_k \approx x_k - \mathrm{i} x_k \left(p_2 \overline{n}_2 + p_1 \overline{n}_1\right) \tau_j \,, \tag{49}$$

$$y'_k \approx y_k - \mathrm{i} y_k \left(p_2 \overline{n}_2 + p_1 \overline{n}_1\right) \tau_j \,, \tag{50}$$

$$\gamma' \approx \gamma - p_1 \left(\overline{n}_2 - \overline{n}_1\right) \tau_j \,, \tag{51}$$

$$\vartheta'_j \approx \vartheta_j + \left(p_2 \overline{n}_2 + p_1 \overline{n}_1 - \omega_j\right) \tau_j \,, \tag{52}$$

with

$$\overline{n}_k = \beta_k^3 \mu_k^2 / \Gamma_k^3 \,. \tag{53}$$

We then replace expressions (50) to (52) into the equations of motion (47) and average over the fast angle γ (as in Eq. (33)) to finally get the secular equations for the tidal evolution

$$\begin{aligned}\dot{x}_1 =& -\frac{3}{2}\frac{\mathcal{D}_{10}}{\Gamma_1^{13}}\Big(\mathrm{i}(2p+5)+(19\overline{n}_1-12\omega_0)\tau_0\Big)x_1\\ &-\frac{3}{2}\frac{\mathcal{D}_{01}}{\Gamma_1^{13}}\Big(\mathrm{i}(2p+5)+(19\overline{n}_1-12\omega_1)\tau_1\Big)x_1\\ &+3\mathrm{i}(p+2)\frac{\mathcal{D}_{20}}{\Gamma_2^{13}}\,x_1+3\mathrm{i}(p+2)\frac{\mathcal{D}_{02}}{\Gamma_2^{13}}\,x_1\,,\end{aligned} \tag{54}$$

$$\begin{aligned}\dot{x}_2 =& -3\mathrm{i}p\frac{\mathcal{D}_{10}}{\Gamma_1^{13}}\,x_2-\frac{3}{2}\frac{\mathcal{D}_{20}}{\Gamma_2^{13}}\Big(\mathrm{i}(1-2p)+(19\overline{n}_2-12\omega_0)\tau_0\Big)x_2\\ &-3\mathrm{i}p\frac{\mathcal{D}_{01}}{\Gamma_1^{13}}\,x_2-\frac{3}{2}\frac{\mathcal{D}_{02}}{\Gamma_2^{13}}\Big(\mathrm{i}(1-2p)+(19\overline{n}_2-12\omega_2)\tau_2\Big)x_2\,,\end{aligned} \tag{55}$$

$$\begin{aligned}\dot{y}_1 =& -\frac{3}{2}\frac{\mathcal{D}_{10}}{\Gamma_1^{13}}\left(2\mathrm{i}p+\overline{n}_1\tau_0\right)y_1+3\mathrm{i}(p+2)\frac{\mathcal{D}_{20}}{\Gamma_2^{13}}\,y_1\\ &-\frac{3}{2}\frac{\mathcal{D}_{01}}{\Gamma_1^{13}}\left(2\mathrm{i}p+\overline{n}_1\tau_1\right)y_1+3\mathrm{i}(p+2)\frac{\mathcal{D}_{02}}{\Gamma_2^{13}}\,y_1\,,\end{aligned} \tag{56}$$

$$\begin{aligned}\dot{y}_2 =& -3\mathrm{i}p\frac{\mathcal{D}_{10}}{\Gamma_1^{13}}\,y_2+\frac{3}{2}\frac{\mathcal{D}_{20}}{\Gamma_2^{13}}\big(2\mathrm{i}(p+2)-\overline{n}_2\tau_0\big)y_2\\ &-3\mathrm{i}p\frac{\mathcal{D}_{01}}{\Gamma_1^{13}}\,y_2+\frac{3}{2}\frac{\mathcal{D}_{02}}{\Gamma_2^{13}}\big(2\mathrm{i}(p+2)-\overline{n}_2\tau_2\big)y_2\,,\end{aligned} \tag{57}$$

$$
\begin{aligned}
\dot{\Gamma} = & 3\frac{\mathcal{D}_{10}}{\Gamma_1^{13}}\left(1+\frac{2}{p}\right)\Big[\left(27x_1\bar{x}_1 - y_1\bar{y}_1 + 6p(x_1\bar{x}_1 + x_2\bar{x}_2 + y_1\bar{y}_1 + y_2\bar{y}_2) + \Gamma_1\right)\omega_0 \\
& - \left(46x_1\bar{x}_1 + 6p(x_1\bar{x}_1 + x_2\bar{x}_2 + y_1\bar{y}_1 + y_2\bar{y}_2) + \Gamma_1\right)\bar{n}_1\Big]\tau_0 \\
& + 3\frac{\mathcal{D}_{01}}{\Gamma_1^{13}}\left(1+\frac{2}{p}\right)\Big[\left(27x_1\bar{x}_1 - y_1\bar{y}_1 + 6p(x_1\bar{x}_1 + x_2\bar{x}_2 + y_1\bar{y}_1 + y_2\bar{y}_2) + \Gamma_1\right)\omega_1 \\
& - \left(46x_1\bar{x}_1 + 6p(x_1\bar{x}_1 + x_2\bar{x}_2 + y_1\bar{y}_1 + y_2\bar{y}_2) + \Gamma_1\right)\bar{n}_1\Big]\tau_1 \\
& + 3\frac{\mathcal{D}_{20}}{\Gamma_2^{13}}\left(1+\frac{2}{p}\right)\Big[\Big(27x_2\bar{x}_2 - y_2\bar{y}_2 - 6(p+2)(x_1\bar{x}_1 + x_2\bar{x}_2 + y_1\bar{y}_1 + y_2\bar{y}_2) + \Gamma_2\Big)\omega_0 \\
& - \left(46x_2\bar{x}_2 - 6(p+2)(x_1\bar{x}_1 + x_2\bar{x}_2 + y_1\bar{y}_1 + y_2\bar{y}_2) + \Gamma_1\right)\bar{n}_2\Big]\tau_0 \\
& + 3\frac{\mathcal{D}_{02}}{\Gamma_2^{13}}\left(1+\frac{2}{p}\right)\Big[\Big(27x_2\bar{x}_2 - y_2\bar{y}_2 - 6(p+2)(x_1\bar{x}_1 + x_2\bar{x}_2 + y_1\bar{y}_1 + y_2\bar{y}_2) + \Gamma_2\Big)\omega_2 \\
& - \left(46x_2\bar{x}_2 - 6(p+2)(x_1\bar{x}_1 + x_2\bar{x}_2 + y_1\bar{y}_1 + y_2\bar{y}_2) + \Gamma_1\right)\bar{n}_2\Big]\tau_2 \,,
\end{aligned}
\tag{58}
$$

$$
\begin{aligned}
\dot{\Theta}_0 = & -3\frac{\mathcal{D}_{10}}{\Gamma_1^{13}}\Big[\left(15x_1\bar{x}_1 - y_1\bar{y}_1 + 6p(x_1\bar{x}_1 + x_2\bar{x}_2 + y_1\bar{y}_1 + y_2\bar{y}_2) + \Gamma_1\right)\omega_0 \\
& - \left(27x_1\bar{x}_1 - y_1\bar{y}_1 + 6p(x_1\bar{x}_1 + x_2\bar{x}_2 + y_1\bar{y}_1 + y_2\bar{y}_2) + \Gamma_1\right)\bar{n}_1\Big]\tau_0 \\
& - 3\frac{\mathcal{D}_{20}}{\Gamma_2^{13}}\Big[\left(15x_2\bar{x}_2 - y_2\bar{y}_2 - 6(p+2)(x_1\bar{x}_1 + x_2\bar{x}_2 + y_1\bar{y}_1 + y_2\bar{y}_2) + \Gamma_2\right)\omega_0 \\
& - \left(27x_2\bar{x}_2 - y_2\bar{y}_2 - 6(p+2)(x_1\bar{x}_1 + x_2\bar{x}_2 + y_1\bar{y}_1 + y_2\bar{y}_2) + \Gamma_2\right)\bar{n}_2\Big]\tau_0 \,,
\end{aligned}
\tag{59}
$$

$$
\begin{aligned}
\dot{\Theta}_1 = & -3\frac{\mathcal{D}_{01}}{\Gamma_1^{13}}\Big[\left(15x_1\bar{x}_1 - y_1\bar{y}_1 + 6p(x_1\bar{x}_1 + x_2\bar{x}_2 + y_1\bar{y}_1 + y_2\bar{y}_2) + \Gamma_1\right)\omega_1 \\
& - \left(27x_1\bar{x}_1 - y_1\bar{y}_1 + 6p(x_1\bar{x}_1 + x_2\bar{x}_2 + y_1\bar{y}_1 + y_2\bar{y}_2) + \Gamma_1\right)\bar{n}_1\Big]\tau_1 \,,
\end{aligned}
\tag{60}
$$

$$
\begin{aligned}
\dot{\Theta}_2 = & -3\frac{\mathcal{D}_{02}}{\Gamma_2^{13}}\Big[\left(15x_2\bar{x}_2 - y_2\bar{y}_2 - 6(p+2)(x_1\bar{x}_1 + x_2\bar{x}_2 + y_1\bar{y}_1 + y_2\bar{y}_2) + \Gamma_2\right)\omega_2 \\
& - \left(27x_2\bar{x}_2 - y_2\bar{y}_2 - 6(p+2)(x_1\bar{x}_1 + x_2\bar{x}_2 + y_1\bar{y}_1 + y_2\bar{y}_2) + \Gamma_2\right)\bar{n}_2\Big]\tau_2 \,,
\end{aligned}
\tag{61}
$$

where

$$
\mathcal{D}_{ij} = k_{2,j}\mathcal{G}m_i^2\beta_k^{12}\mu_k^6 R_j^5 \quad \text{with} \quad k = \max(i,j)\,. \tag{62}
$$

We note that in the expressions of $\dot{x}_k$ (Eqs. (54) and (55)) and $\dot{y}_k$ (Eq. (56) and (57)), we have a conservative contribution (imaginary terms) and a dissipative contribution (real terms in τ_j). The conservative contributions result from a permanent tidal deformation and only slightly modify the fundamental frequencies of the system, while the dissipative contributions modify the secular evolution.

Tidal dissipation induce variations in the parameters Γ (Eq. (58)) and Θ_k (Eqs. (59)−(61)). Then, the coefficients $\mathcal{K}$, $\mathcal{O}$, $\mathcal{S}$ and $\mathcal{R}$ appearing in the Hamiltonian (37) slowly change in time (Eqs. (26)−(27)), which translates into a secular evolution of the system. We also note that for the oblateness terms (Eqs. (98)−(101)), changes are observed not only due to Γ, but also in J_2 because of the evolution of Uranus' rotation rate, $\omega_0 = \Theta_0/C_0$ (Eq. (2)).

4. Planar dynamics

Tittemore and Wisdom (1988) have studied the passage through the 5/3 MMR between Ariel and Umbriel using a secular planar two-satellite model, which has only two degrees-of-freedom. To better compare with our results, in this section we also restrict our model to the planar case ($I_k = 0$). This is equivalent to set $y_k = 0$, which suppresses the terms in $\mathcal{O}_3$, $\mathcal{O}_4$, $\mathcal{S}_5$, $\mathcal{S}_6$, $\mathcal{S}_7$, $\mathcal{R}_4$, $\mathcal{R}_5$, and $\mathcal{R}_6$ in the resonant secular Hamiltonian (Eq. (37)) and further simplifies the terms in $\mathcal{K}_1$, $\mathcal{K}_2$, and $\mathcal{S}_1$, yielding to

$$\begin{aligned}\bar{\mathcal{H}} &= (\mathcal{K}_1 + \mathcal{S}_1)\left(x_1\bar{x}_1 + x_2\bar{x}_2\right) + \mathcal{K}_2\left(x_1\bar{x}_1 + x_2\bar{x}_2\right)^2 \\ &+ (\mathcal{O}_1 + \mathcal{S}_2)x_1\bar{x}_1 + (\mathcal{O}_2 + \mathcal{S}_3)x_2\bar{x}_2 + \frac{\mathcal{S}_4}{2}\left(x_1\bar{x}_2 + \bar{x}_1x_2\right) \\ &+ \frac{\mathcal{R}_1}{2}\left(x_1^2 + \bar{x}_1^2\right) + \frac{\mathcal{R}_2}{2}\left(x_2^2 + \bar{x}_2^2\right) + \frac{\mathcal{R}_3}{2}\left(x_1x_2 + \bar{x}_1\bar{x}_2\right) \ .\end{aligned} \tag{63}$$

The values of m_k, J_2, and R_0 are relatively well determined for the Uranian system (Table 1). Therefore, to compute the remaining coefficients $\mathcal{K}$, $\mathcal{O}$, $\mathcal{S}$, and $\mathcal{R}$ appearing in the Hamiltonian (Eq. (37)), we only need to know the values of the parameters Γ_1 and Γ_2 (see Appendix A), which in turn depend on the parameters Γ and Δ (Eq. (26)).

In Paper I, we performed a backwards tidal evolution of the semi-major axes of Ariel and Umbriel, and estimated that the 5/3 MMR between Ariel and Umbriel was crossed about 640 Myr ago, with

$$a_1/R_0 = 7.39054 \quad \text{and} \quad a_2/R_0 = 10.38909 \, . \tag{64}$$

Adopting these semi-major axes and considering for simplicity $e_k = I_k = 0$, we obtain (Eq. (21))

$$\Gamma = 2.647\,289 \times 10^{-12} \ \mathrm{M_\odot\,au^2\,yr^{-1}} \ . \tag{65}$$

The conservative dynamics is not very sensitive to the Γ parameter (eg. Tittemore and Wisdom, 1988, 1989), and so we fix it at the reference value estimated for the near resonance encounter (Eq. (65)).

The dynamics of the 5/3 MMR thus mainly depends on the Δ-parameter (Eq. (27)), which measures the proximity to the resonance. Following Delisle et al. (2012) and Gomes and Correia (2023), we write

$$\delta = \frac{\Delta}{\Delta_r} - 1 \ , \tag{66}$$

where Δ_r is the value of Δ at the circular planar ($e_k = I_k = 0$) nominal resonance, that is (Eq. (19) and (27)),

$$\Delta_r = \left(\Lambda_{1,r} + \Lambda_{2,r}\right)/\Gamma_r \ , \tag{67}$$

when $n_1/n_2 = 5/3$, where n_k is the mean motion of the satellite with mass m_k. At the nominal resonance, using Kepler's third law, we have (Gomes and Correia, 2023)

$$\Delta_r = \left(1 + \epsilon\left(\tfrac{5}{3}\right)^{1/3}\right)\left(\tfrac{5}{3} + \epsilon\left(\tfrac{5}{3}\right)^{1/3}\right)^{-1} \ , \quad \text{with} \quad \epsilon \approx \frac{m_2}{m_1} \ . \tag{68}$$

4.1. Equilibrium points

The equilibrium points correspond to stationary solutions of the Hamiltonian. They can be found by solving

$$\frac{\partial\bar{\mathcal{H}}}{\partial x_1} = 0 \quad \text{and} \quad \frac{\partial\bar{\mathcal{H}}}{\partial x_2} = 0 \, , \tag{69}$$

which correspond to the roots of equations (39) and (40) with $y_k = 0$. Splitting these equations in their real and imaginary parts, $x_k = x_{k,r} + \mathrm{i}x_{k,i}$, and following a similar procedure as in Gomes and Correia (2023), we find that

stable equilibria can only occur when the real roots are null, i.e., $x_{1,r} = x_{2,r} = 0$. We then focus on the imaginary roots to determine the exact position of the stable equilibria. Since $x_{1,r} = x_{2,r} = 0$, we have (Eq. (35))

$$x_{1,i} = \pm\sqrt{\Sigma_1} \quad \text{and} \quad x_{2,i} = \pm\sqrt{\Sigma_2}\,, \tag{70}$$

with

$$\Sigma_1 = \Sigma_2 = 0\,, \tag{71}$$

or

$$\Sigma_1 = \frac{(\mathcal{R}_3 - \mathcal{S}_4)\varepsilon_\pm - 2(\mathcal{K}_1 + \mathcal{O}_1 + \mathcal{S}_1 + \mathcal{S}_2 - \mathcal{R}_1)}{4\mathcal{K}_2(1+\varepsilon_\pm^2)}\,, \tag{72}$$

$$\Sigma_2 = \varepsilon_\pm^2\,\Sigma_1\,, \tag{73}$$

where

$$\begin{aligned}\varepsilon_\pm =& \frac{\mathcal{O}_1 - \mathcal{O}_2 - \mathcal{R}_1 + \mathcal{R}_2 + \mathcal{S}_2 - \mathcal{S}_3}{\mathcal{R}_3 - \mathcal{S}_4} \\ &\pm \frac{\sqrt{(\mathcal{O}_1 - \mathcal{O}_2 - \mathcal{R}_1 + \mathcal{R}_2 + \mathcal{S}_2 - \mathcal{S}_3)^2 + (\mathcal{R}_3 - \mathcal{S}_4)^2}}{\mathcal{R}_3 - \mathcal{S}_4}\,.\end{aligned} \tag{74}$$

The equilibrium point at $\Sigma_1 = \Sigma_2 = 0$ (Eq. (71)) is always present, although it can be stable or unstable. The remaining equilibria (Eqs. (72)–(74)) only exist for some δ-values. In Fig. 1, we show the evolution of the equilibrium points as a function of δ. We rescale $x_{k,i}$ by $\sqrt{\Gamma_k/2}$, such that we can translate the different equilibria in terms of eccentricities (Eq. (36)).

For positive δ values far from zero, there is only one equilibrium point at $e_k = 0$, which is stable (in blue colour). For $\delta = 1.2 \times 10^{-6}$, there is a first bifurcation in the equilibria: two new stable equilibrium appear at non-zero inclination (in green colour), while the point at $e_k = 0$ becomes unstable. For $\delta = -3.7 \times 10^{-6}$, which is close to the resonance nominal value $\delta = 0$ (Eq. (67)), a second bifurcation arises: two additional unstable equilibrium points appear at non-zero eccentricity (in red colour), while the point at $e_k = 0$ becomes stable again. This distribution of the equilibrium points is very similar to the one obtained for the secular resonant two-satellite circular model with low inclinations (see Fig. 1 in Gomes and Correia, 2023).

4.2. Energy levels

For a deeper understanding of the dynamics, we can examine the energy levels of the resonant planar Hamiltonian (Eq. (63)) for various values of δ (Eq. (68)). Given that our problem involves two degrees of freedom, thus four dimensions, we need to depict these levels on sectional planes. To ensure that all stable equilibria are visible, we choose the plane $(x_{1,i}, x_{2,i})$ with $x_{1,r} = x_{2,r} = 0$ (Eq. (70)). In Fig. 2, we show the energy levels for three distinct values of δ, each representative of the three equilibrium possibilities depicted in Fig. 1. Once more, we rescale the $x_{k,i}$ by $\sqrt{\Gamma_k/2}$, and so we actually show the energy levels in the plane $(e_1 \sin\sigma_1, e_2 \sin\sigma_2)$ with $\cos\sigma_1 = \cos\sigma_2 = 0$. We observe that this figure is also very similar to the one obtained for the secular resonant two-satellite circular model with low inclinations (see Fig. 2 in Gomes and Correia, 2023), although here the energy levels symmetry axis is more tilted.

For $\delta = 5 \times 10^{-6} > 0$ (Fig. 2 a) there is a single equilibrium point ($x_{1,i} = 0, x_{2,i} = 0$) at the centre (in blue). It corresponds to a fix point of the planar Hamiltonian (Eq. (63)), encircled by a circulating region. Therefore, in this case (and for higher δ-values), all trajectories lie outside the 5/3 MMR

For $\delta = 0$ (Fig. 2 b), the system is at the nominal resonance (Eq. (66)). Here, the equilibrium point at the centre ($x_{1,i} = 0, x_{2,i} = 0$) is still present (in red), yet it becomes unstable. Notably, a separatrix in a tilted 8-shape emerges from this point, encompassing two additional stable equilibrium points (depicted in green). Trajectories inside the separatrix that encircle the stable points are in libration and correspond to orbits inside the 5/3 MMR. Trajectories outside the separatrix are in circulation.

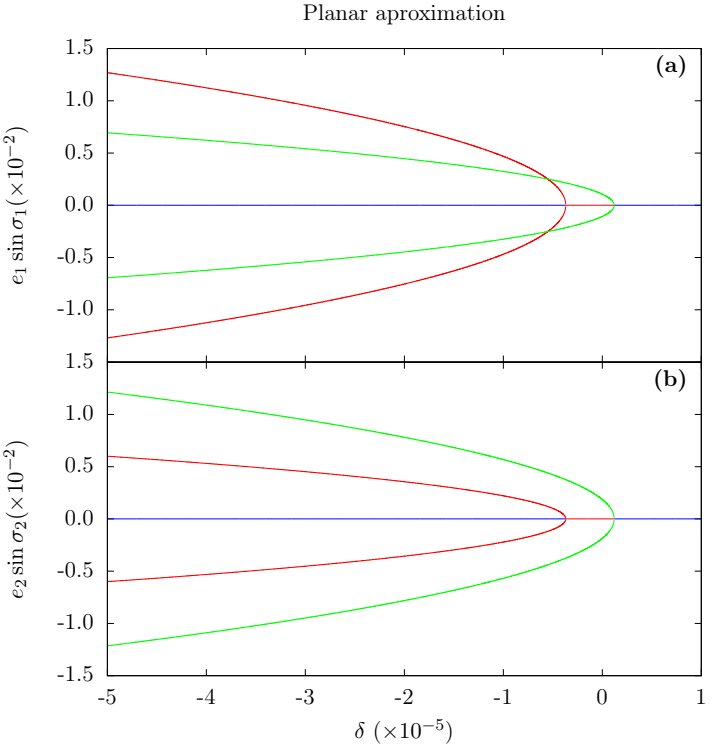

Figure 1: Evolution of the equilibrium points as function of δ. The green lines represent stable points inside the resonance (in a libration region), the red lines represent hyperbolic points (unstable), and the blue lines represent stable fixed points (in a circulation region).

Finally, for $\delta = -5 \times 10^{-6} < 0$ (Fig. 2 c), five equilibrium points exist. Two hyperbolic points (depicted in red) give rise to a separatrix with two 'banana' shapes. This separatrix delineates the phase space into regions of libration and circulation. There are two stable points (in green), one inside each banana island. Trajectories revolving around these points undergo libration and correspond to orbits within the 5/3 MMR. The center point ($x_{1,i} = 0, x_{2,i} = 0$) (in blue) is again stable and inside a small circulation region. Trajectories outside the separatrix are also in circulation. This phase space configuration persists for smaller δ-values, but the central circulation region becomes larger, while the resonant islands become smaller.

4.3. Capture probabilities

Understanding the system's behaviour upon crossing the 5/3 MMR is not straightforward due to the problem's two degrees of freedom. To gain insight into the critical eccentricities that either trap the system in resonance or allow to skip it, we can construct a simplified one-degree-of-freedom model and estimate the capture probability for various eccentricities, following Tittemore and Wisdom (1988).

Using the same method described in Gomes and Correia (2023) to study the effect of inclination on the capture probability of the 5/3 MMR between Ariel and Umbriel, we obtain the capture probability as a function of the eccentricity,

$$P_{\rm cap} = 1 + \frac{\partial \mathcal{J}_k^-}{\partial \Gamma} \Big/ \frac{\partial \mathcal{J}_k^+}{\partial \Gamma} \,, \tag{75}$$

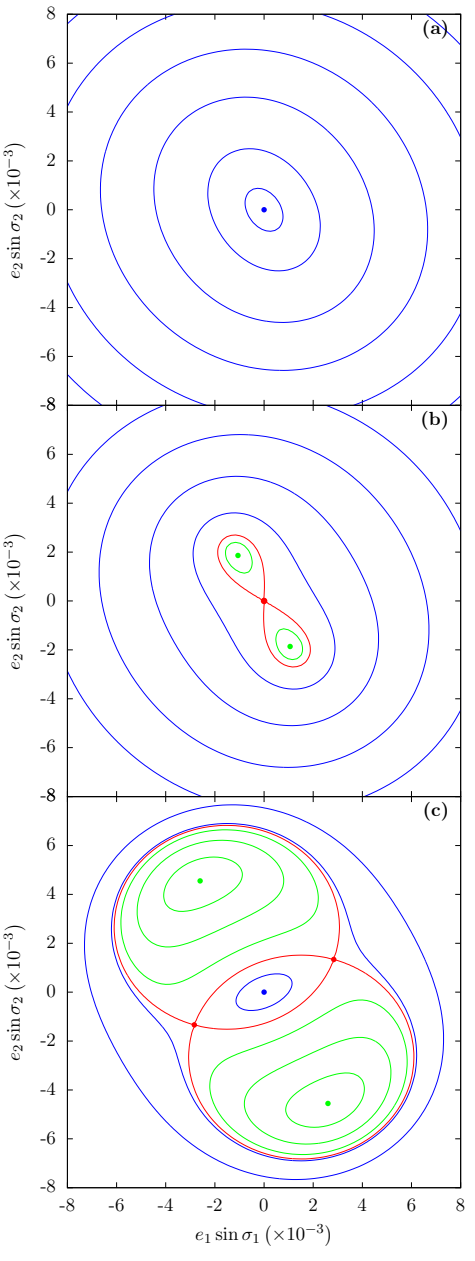

Figure 2: Energy level curves in the plane $(e_1 \sin\sigma_1, e_2 \sin\sigma_2)$ with $\cos\sigma_1 = \cos\sigma_2 = 0$, for $\delta = 5 \times 10^{-6}$ (top), $\delta = 0$ (middle), and $\delta = -5 \times 10^{-6}$ (bottom). Stable equilibria are coloured in green (libration) and blue (circulation), while unstable equilibria are coloured in red, as well as the level curves that correspond to the separatrix.

where,

$$\frac{\partial \mathcal{J}_k^-}{\partial \Gamma} = \frac{1}{\mathcal{B}_k^2}\left(\arcsin\left(\sqrt{-\frac{\mathcal{C}_k}{\mathcal{A}_k}}\right) + \frac{\pi}{2}\right)(\mathcal{B}_k\mathcal{A}_k' - \mathcal{A}_k\mathcal{B}_k') + \frac{1}{\mathcal{B}_k^2}\sqrt{-\frac{\mathcal{C}_k + \mathcal{A}_k}{\mathcal{C}_k}}(\mathcal{B}_k\mathcal{C}_k' - \mathcal{C}_k\mathcal{B}_k')\,, \tag{76}$$

$$\frac{\partial \mathcal{J}_k^+}{\partial \Gamma} = \frac{1}{\mathcal{B}_k^2}\left(\arcsin\left(\sqrt{-\frac{\mathcal{C}_k}{\mathcal{A}_k}}\right) - \frac{\pi}{2}\right)(\mathcal{B}_k\mathcal{A}_k' - \mathcal{A}_k\mathcal{B}_k') + \frac{1}{\mathcal{B}_k^2}\sqrt{-\frac{\mathcal{C}_k + \mathcal{A}_k}{\mathcal{C}_k}}(\mathcal{B}_k\mathcal{C}_k' - \mathcal{C}_k\mathcal{B}_k')\,, \tag{77}$$

and $\mathcal{A}_k' = \partial\mathcal{A}_k/\partial\Gamma$, $\mathcal{B}_k' = \partial\mathcal{B}_k/\partial\Gamma$, and $\mathcal{C}_k' = \partial\mathcal{C}_k/\partial\Gamma$. Note that since Γ is the only time dependent quantity in the expressions of $\mathcal{A}_k$, $\mathcal{B}_k$, and $\mathcal{C}_k$ (appendix A), $\dot{\mathcal{J}}_k = \dot{\Gamma}\,\partial\mathcal{J}_k/\partial\Gamma$ (we neglect the small changes in Θ from the oblateness terms, $\mathcal{O}_k$). For the eccentricity, the single resonance terms are

$$\bar{\mathcal{H}}_k = \mathcal{A}_k x_k \bar{x}_k + \mathcal{B}_k\left(x_k\bar{x}_k\right)^2 + \mathcal{C}_k/2\left(x_k^2 + \bar{x}_k^2\right) \tag{78}$$

with

$$\mathcal{A}_1 = \mathcal{K}_1 + \mathcal{O}_1 + \mathcal{S}_1 + \mathcal{S}_2\,, \quad \mathcal{B}_1 = \mathcal{K}_2\,, \quad \mathcal{C}_1 = \mathcal{R}_1\,, \tag{79}$$

$$\mathcal{A}_2 = \mathcal{K}_1 + \mathcal{O}_2 + \mathcal{S}_1 + \mathcal{S}_3\,, \quad \mathcal{B}_2 = \mathcal{K}_2\,, \quad \mathcal{C}_2 = \mathcal{R}_2\,. \tag{80}$$

In Fig. 3, we show the probability of capture in the σ_1 and σ_2 resonances obtained with expression (75). For some eccentricity values, numerical integrations of the equations of motion derived from the simplified Hamiltonian (Eq. (78)) together with the secular tidal equations (Eqs. (54), (55), and (59)) are also presented. For each initial eccentricity, we ran 100 simulations where the initial angle σ_k is uniformly sampled. The amount of simulations captured in resonance at the end of the simulation are marked with a dot. The statistical fluctuation, represented as error bars, were estimated using binomial statistics. We observe a close correspondence between the theoretical curve (Eq. (75)) and the output of the numerical simulations, i.e, the adiabatic approximation holds. These results align with those presented in Fig. 31 in Tittemore and Wisdom (1988).

In Fig. 3, we observe that for initial eccentricities lower than 0.005 the system is consistently captured in resonance. However, as the initial eccentricity increases, the capture probability quickly decreases, it becomes $\sim$ 40% for $e_k \sim 0.01$. This results suggest that a system with nearly circular orbits is unlikely to escape the 5/3 MMR. Conversely, for eccentricities higher than about 0.01, it may be able to evade it.

We cannot entirely rely on the conclusions drawn from the simplified Hamiltonian, primarily for two reasons. Firstly, the complete planar Hamiltonian (Eq. (63)) depends on the eccentricity of the other body. When we simplified the Hamiltonian (Eq. (78)) for x_1, we omitted all terms involving x_2 (and vice versa), effectively setting $x_2 = 0$. However, if we set $x_2 \neq 0$, additional terms emerge in the Hamiltonian, resulting in a distinct distribution of capture probabilities. Secondly, the complete Hamiltonian has two degrees-of-freedom, and thus, for certain combinations of eccentricity values, the system can exhibit chaotic behaviour (see next section).

4.4. Chaotic diffusion

The energy levels obtained in Sect. 4.2 allow us to identify the different regions of the phase space (Fig. 2), but a priori they do not correspond to trajectories followed by the system. Indeed, since the planar problem has two degrees-of-freedom, hence four dimensions, the energy levels show the trajectories when they cross the section plane with $x_{1,r} = x_{2,r} = 0$, which only remain constant for the equilibrium points. Therefore, to study the global dynamics, in this section we adopt the frequency analysis method (Laskar, 1990, 1993) to map the diffusion of the orbits, as explained in Gomes and Correia (2024b).

In Fig. 2, we observe that the more diverse dynamics occurs for $\delta = -5\times10^{-6}$. We then use this value to draw the diffusion maps. For each map we fix an energy value and build a grid of 200×200 equally distributed initial conditions in the plane $(x_{1,i}, x_{1,r})$. We fix $x_{2,r} = 0$ for all initial conditions and compute $x_{2,i}$ from the total energy (Eq. (63)). Since the planar Hamiltonian is a four-degree function of x_k, the intersection of the constant energy manifold by a plane may have up to four roots (families). Each family corresponds to a different dynamical behaviour, and so we must plot one of them at a time. However, the families are symmetric and actually we only need to show two of them. We chose to

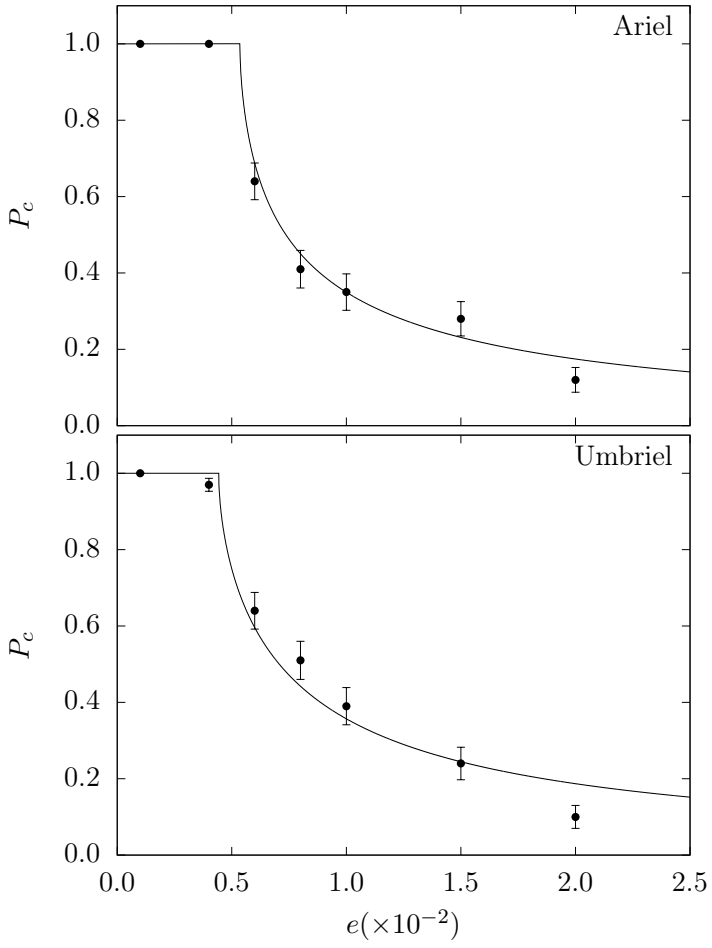

Figure 3: Capture probabilities in the σ_1 (top) and σ_2 (bottom) resonances. The solid line gives the theoretical approximation given by Eq. (75), while the dots give the results of numerical simulations. We ran 100 initial conditions with σ_k differing by 1.8°.

represent the families with the positive roots (that we dub 1 and 2). We then numerically integrate the planar equations of motion (39) and (40), with $y_k = 0$, for a time T. Finally, we perform a frequency analysis of x_1, using the software TRIP (Gastineau and Laskar, 2011) over the time intervals $[0, T/2]$ and $[T/2, T]$, and determine the main frequency in each interval, $f_{\rm in}$ and $f_{\rm out}$, respectively. The stability of the orbit is measured by the index

$$D \equiv \left| 1 - \frac{f_{\rm out}}{f_{\rm in}} \right| , \tag{81}$$

which estimates the stability of the orbital long-distance diffusion (Dumas and Laskar, 1993). The larger D, the more orbital diffusion exists. For stable motion, we have $D \sim 0$, while $D \ll 1$ if the motion is weakly perturbed, and $D \sim 1$ when the motion is irregular. It is difficult to determine the precise value of D for which the motion is stable or unstable, but a threshold of stability D_s can be estimated such that most of the trajectories with $D < D_s$ are stable (for more details see Couetdic et al., 2010). The diffusion index D is represented by a logarithmic colour scale calibrated such that blue and green correspond to quasi-periodic trajectories ($D \ll D_s$), while orange and red correspond to chaotic motion ($D \gg D_s$).

We show the diffusion maps of Ariel for family 1 in Fig. 4 and for family 2 in Fig. 5. We rescaled x_k again by $\sqrt{\Gamma_k/2}$, and so we actually show the surface sections in the plane $(e_1 \sin\sigma_1, e_1 \cos\sigma_1)$ with $\cos\sigma_2 = 0$. Each panel corresponds to a different energy value $\bar{\mathcal{H}}/\mathcal{H}_0$ (Eq. (63)), corresponding to the levels shown in Fig. 2 c, where $\mathcal{H}_0 = 5.789 \times 10^{-20}\ M_\odot\ \mathrm{au}^2\ \mathrm{yr}^{-2}$ is the energy of the of the separatrix. The lowest energies occur in the circulation

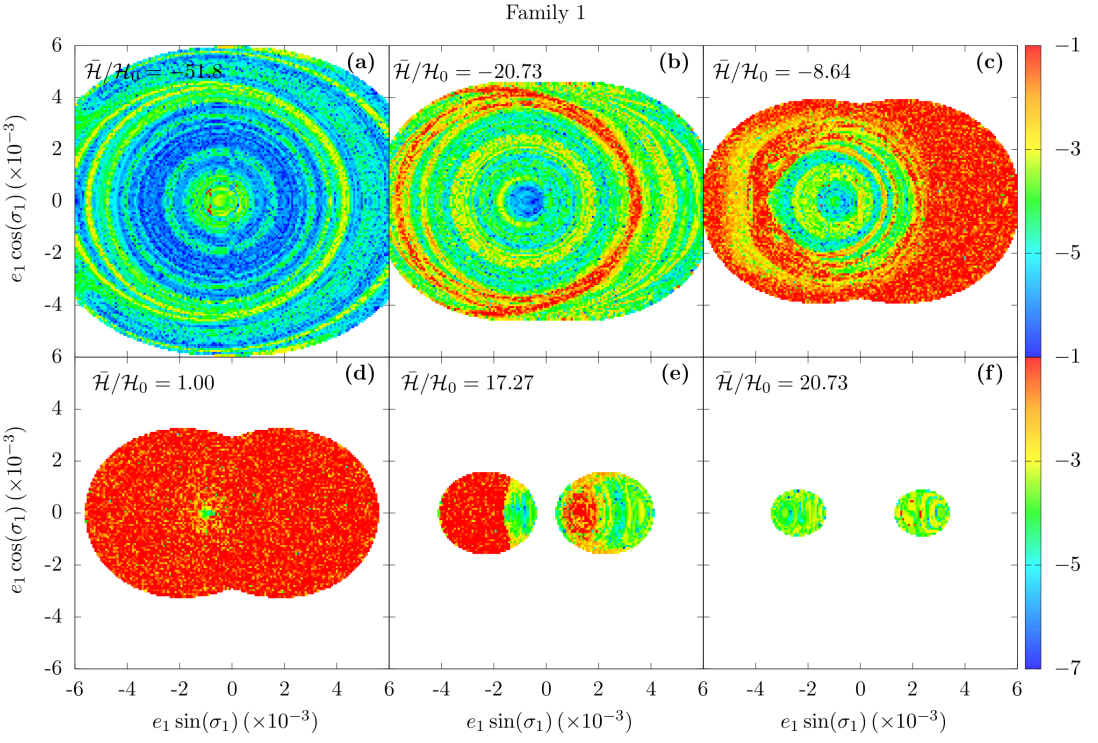

Figure 4: Diffusion maps for Ariel in the plane $(e_1 \sin\sigma_1, e_1 \cos\sigma_1)$ with $\cos\sigma_2 = 0$ and $\delta = -5 \times 10^{-6}$, for trajectories corresponding to family 1. Each panel was obtained with a different energy value, and $\mathcal{H}_0 = 5.789 \times 10^{-20}$ $M_\odot\,au^2\,yr^{-2}$. The colour scale corresponds to the relative frequency diffusion index in logarithmic scale (Eq. (81)). More negative values correspond to stable orbits, while larger values correspond to more chaotic orbits.

regions, $\bar{\mathcal{H}} < \mathcal{H}_0$, while the largest energies occur in the libration region, $\bar{\mathcal{H}} > \mathcal{H}_0$. The inner circulation region is delimited by $0 < \bar{\mathcal{H}} < \mathcal{H}_0$, where $\bar{\mathcal{H}} = 0$ corresponds to the energy of the equilibrium point with $x_1 = x_2 = 0$. For this energy range, there are four families, while for the remaining energies only two families exist.

For $\bar{\mathcal{H}} \ll 0$ (Fig. 4 a), only family 1 exists, and we observe that the system is always quasi-periodic, corresponding to trajectories in the outer circulation region. This corresponds to the blue line trajectories in Fig. 2 c, the outer circulation region. As the energy increases, concentric chaotic regions start to emerge outside the separatrix (Fig. 4 b). These regions become increasingly dominant with the increase of the energy, initially maintaining a small region near the stable internal circulation zone (Fig. 4 c).

As the energy becomes positive, $\bar{\mathcal{H}} > 0$, that is, as we enter the inner circulation region, the stable internal circulation zone becomes increasingly smaller, up to $\bar{\mathcal{H}} = \mathcal{H}_0$ (red line trajectories of Fig. 2 c), were the phase space is completely dominated by chaotic trajectories (Fig. 4 d). For $0 < \bar{\mathcal{H}} < \mathcal{H}_0$, family 2 also exists (Fig. 5). Yet, it maintains the regime observed in the separatrix, with chaos dominating all trajectories.

Finally, for $\bar{\mathcal{H}} \gg \mathcal{H}_0$, that is, as we enter the green resonance regions of Fig. 2 c, two resonant islands emerge. Here, the phase-space can be stable again (Fig. 4 e), and confined to small eccentricity ranges. For $\bar{\mathcal{H}}$ close to the libration centers, the trajectories are fully stable and quasi-periodic (Fig. 4 f).

From the analysis of the planar diffusion maps, we conclude that, as for the circular dynamics (Gomes and Correia, 2023, 2024b), the planar dynamics of the 5/3 MMR between Ariel and Umbriel is highly intricate and contingent upon the energy of the system. In fact, the energy depends on the value of the eccentricities (Eq. (63)), given by the variables x_1 and x_2 (Eq. (36)). Therefore, the value of the eccentricity of Ariel and Umbriel when the system encounters the resonance can trigger completely different behaviours. For $\bar{\mathcal{H}} \ll 0$, the motion is quasi-periodic. Still, for a wide range of energies close to the separatrix, and mainly for $\bar{\mathcal{H}} \sim \mathcal{H}_0$, the motion is mostly chaotic. Only for $\bar{\mathcal{H}} \gg \mathcal{H}_0$, the motion is again quasi-periodic, but only possible in libration with a small amplitude around the high eccentricity stable equilibrium points (Fig. 1).

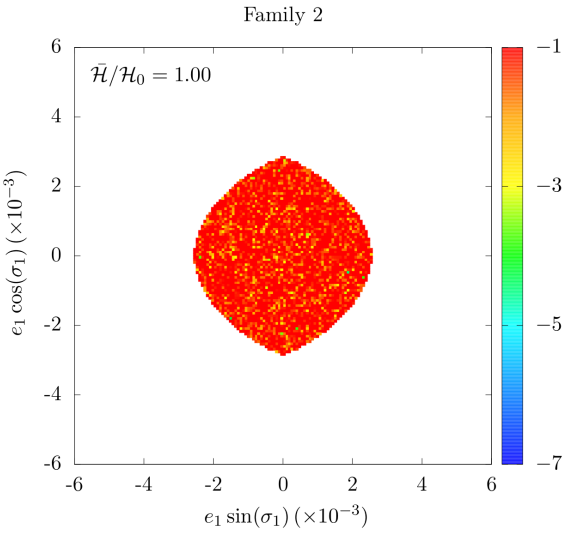

Figure 5: Diffusion map for Ariel in the plane $(e_1 \sin\sigma_1, e_1 \cos\sigma_1)$ with $\cos\sigma_2 = 0$ and $\delta = -5 \times 10^{-6}$, for trajectories corresponding to family 2 and $\bar{\mathcal{H}} = \mathcal{H}_0 = 5.789 \times 10^{-20}$ $\mathrm{M}_\odot\,\mathrm{au}^2\,\mathrm{yr}^{-2}$. The colour scale is the same from Fig. 4.

4.5. Statistics

Owing to the chaotic diffusion, the passage of Ariel and Umbriel through the 5/3 MMR is a stochastic problem. Depending on the initial eccentricity of these satellites, the system may experience quite different evolutions (Sect. 4.4). For the trajectories crossing the chaotic regions, the final outcome is unpredictable and can only be accessed using a large number of numerical simulations to have an accurate statistics of all possible scenarios. Therefore, in this section we integrate the conservative differential equations (39) and (40) together with the dissipative tidal equations (54), (55), and (58) to (61) with $y_k = 0$ (planar motion).

4.5.1. Setup

When the 5/3 MMR is crossed, we cannot perform a backwards integration. We need to place the system slightly before the resonance encounter and then integrate it forwards. It is not possible to determine the exact semi-major axes prior to resonance crossing. Nonetheless, if the system does not spend much time in resonance, the semi-major axes should not differ much from the nominal values (Eq. (64)). We still need to slightly decrease a_1 (or increase a_2) to move the system out of the nominal resonance. Since tides are stronger in Ariel, we opted to shift a_1 and keep a_2 constant:

$$a_1/R_0 = 7.3868\,, \quad a_2/R_0 = 10.3891\,. \tag{82}$$

These values of the semi-major axes allow us to compute the initial Γ parameter (Eq. (19)). For a given set of initial eccentricity values, we then also compute the initial value of Δ (Eq. (27)), which translates into an initial $\delta > 0$ (Eq. (66)).

The physical properties of Uranus and its satellites can be found in Table 1, while the constant Σ parameter is conserved and can also be obtained from the present system (Eq. (20)),

$$\Sigma = 9.367\,247 \times 10^{-10}\ \mathrm{M}_\odot\,\mathrm{au}^2\,\mathrm{yr}^{-1}\,. \tag{83}$$

The initial rotation rate of Uranus is obtained from the conservation of Σ (Eq. (20)), together with Eqs. (24) and (25),

$$\omega_0 = \frac{1}{C_0}\left(\Sigma - \Gamma_1 - \Gamma_2 - \Theta_1 - \Theta_2\right)\,, \tag{84}$$

where the Γ_k (Eq. (10)) are obtained with the pre-resonance semi-major axes (Eq. (82)), and the rotation rate of the satellites is assumed to be synchronous with the orbital period, that is, $\Theta_k = C_k n_k$ (Eq. (9)).

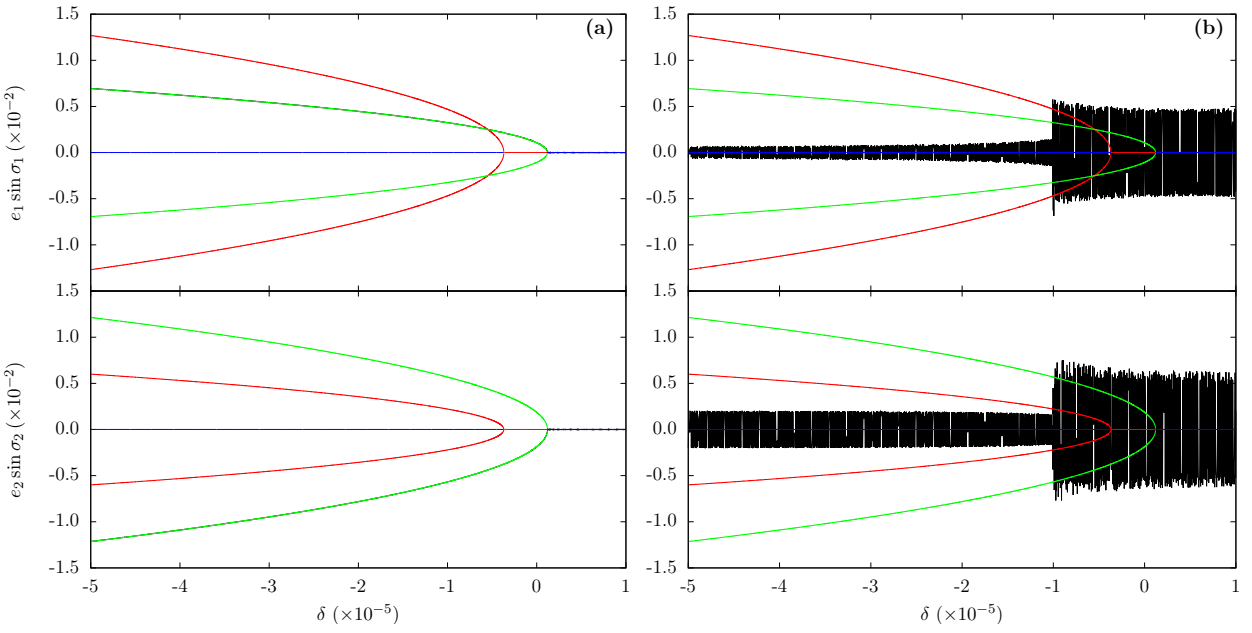

Figure 6: Two examples of tidal evolution of the system as a function of δ for small initial $e_1 = e_2 = 10^{-5}$ (a) and higher initial $e_1 = e_2 = 0.005$ (b). The results of the numerical simulations (in black) are superimposed in the equilibria map for the eccentricity (Fig. 1). We show the evolution for the resonant angle σ_1 (top) and σ_2 (bottom). The results as a function of time must be read from the right to the left.

Finally, for the tidal dissipation of Uranus, we adopt $k_{2,0} = 0.104$ (Gavrilov and Zharkov, 1977) and $\tau_0 = 0.617$ s (corresponding to $Q_0 = 8\,000$, see Sect. 3.1 in Paper I for details), which translates into

$$k_{2,0}\,\tau_0 = 0.064\,\mathrm{s}\,. \tag{85}$$

As for the satellites, we adopt $k_{2,1} = 1.02 \times 10^{-2}$ and $k_{2,2} = 7.35 \times 10^{-2}$ (Chen et al., 2014), together with $\tau_1 = 69.3$ s and $\tau_2 = 113.9$ s (corresponding to $Q_k = 500$, see Sect. 3.2 in Paper I for details), yielding to

$$k_{2,1}\,\tau_1 = 0.707\,\mathrm{s}\,, \quad \text{and} \quad k_{2,2}\,\tau_2 = 0.837\,\mathrm{s}\,. \tag{86}$$

4.5.2. Comparison with analytical estimations

Tidal effects are usually weak and introduce only a small drift in the phase space of the resonant dynamics. To verify that the adiabatic approximation holds in the planar case, we ran two numerical simulations with different initial conditions and then superimposed the output in the equilibria map as a function of δ (Fig. 1). The results are shown in Fig. 6. Since $\omega_0/n_k > 1$, tidal effects are expected to increase the value of Γ (Eq. (58)) and thus decrease the value of δ (Eq. (66)). Therefore, the results as a function of time must be read from the right to the left.

In Fig. 6 a, we adopted very small initial eccentricities for both satellites, $e_1 = e_2 = 10^{-5}$. At the beginning of the simulation, when $\delta > 0$, the system is in circulation with a small amplitude around the equilibrium point at zero ($x_1 = 0, x_2 = 0$). For $\delta \approx 0$, the system encounters the 5/3 MMR and two stable equilibrium points emerge, while the equilibrium point at zero becomes unstable. Because the amplitude of oscillation is small, the system is forced to follow one of the two resonance branches. Therefore, as the system evolves with $\delta < 0$, the eccentricities increase. For initially near circular orbits, it is then impossible to avoid capture in the 5/3 MMR (see also Sect. 4.3).

In Fig. 6 b, we adopted higher initial eccentricities for both satellites, $e_1 = e_2 = 0.005$. The initial evolution for $\delta > 0$ is similar to the case with lower initial eccentricities, except that the amplitude of oscillation is 500 times larger in this case. Therefore, as the system encounters the resonance at $\delta \approx 0$, it is not able to follow one of the resonant branches and it remains in a chaotic region around the separatrix (see Sect. 4.4). After some time in the chaotic region with $\delta < 0$, the inner circulation region around the equilibrium point at zero becomes again stable, and the system finds a way there. We thus confirm that for orbits with some initial eccentricity, the system can experience a chaotic regime for some time, after which it can escape the 5/3 MMR (Tittemore and Wisdom, 1988; Ćuk et al., 2020).

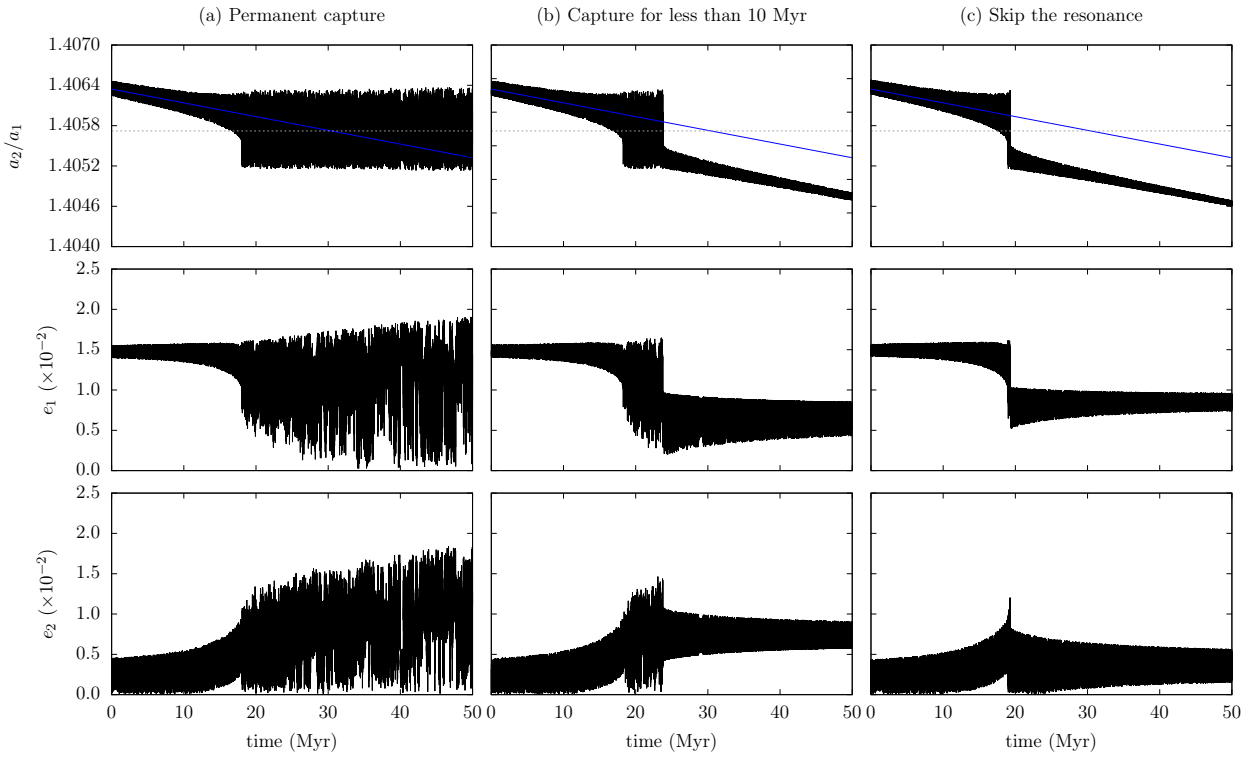

Figure 7: Three examples of a system crossing the 5/3 MMR with initial $e_1 = 0.015$ and $e_2 = 0.005$. We plot the ratio between the semi-major axes (top), the eccentricity of Ariel (middle), and the eccentricity of Umbriel (bottom) as a function of time. Each column corresponds to a different simulation. We show an example of a system that is permanently caught in resonance (a), one that is captured but evades the resonance in less than 10 Myr (b), and another that skips the resonance without capture (c). The blue line gives the asymptotic evolution (see Sect. 3.1 in Paper I), while the dashed line gives the position of the nominal resonance (Eq. (64)).

4.5.3. Results

We explored a mesh of initial eccentricities ranging between 10^{-5} up to 0.020, with a stepsize of 0.005. For each pair (e_1, e_2), we integrated a set of 1 000 simulations evenly sampled over the resonance angle σ (Eq. (13)), over 100 Myr, in a total of 25 000 experiments.

The outcome of the resonance crossing is similar to the one for the circular approximation (Gomes and Correia, 2023), although now it takes place whenever at least one resonant angles, σ_k (Eq. (19)), switches from circulation to libration. We observe that the trajectories can: a) be permanently captured for 100 Myr; b) be captured but escape in less than 100 Myr; or c) quickly skip the resonance. In Fig. 7, we show one example of each kind (for initial $e_1 = 0.015$ and $e_2 = 0.005$).

For each simulation, we evaluated whether capture in resonance occurred by analysing if the semi-major axis ratio a_2/a_1 becomes constant or close to the nominal resonance value (Eq. (64)). We consider that a trajectory escapes the resonance when it skips the resonance, or it is captured for less than 10 Myr (for more details see Gomes and Correia, 2023). In Table 2, we show a summary of the outcome of the resonance crossing for all the initial conditions explored.

We observe that for initial eccentricities of Ariel, e_1, smaller than 0.005, the satellites are always captured in the 5/3 MMR, preventing a future evolution to the currently observed system. These results confirm those obtained by Tittemore and Wisdom (1988). They are also in agreement with the estimations of the capture probability computed with a one degree-of-freedom simplified model (Fig. 3). On the other hand, contrarily to previous analysis, we note that for $e_1 \lesssim 0.005$, the initial eccentricity of Umbriel does not seem to have a significant impact in the number of resonance crossings.

For $e_1 \gtrsim 0.01$, we find that the escape probability increases with the initial eccentricity of Ariel. The number of escapes can attain values as high as 80% for $e_1 = 0.02$. Nevertheless, these numbers are only maximised for small

Table 2
Escape probability from the 5/3 MMR between Ariel-Umbriel for different initial eccentricities (e_1, e_2) assuming a planar model.

e_1 \ e_2	10^{-5}	0.005	0.010	0.015	0.020
10^{-5}	0.0	0.0	0.0	0.0	2.1
0.005	0.0	0.1	0.5	0.2	0.1
0.010	21.9	31.8	25.5	15.8	8.5
0.015	56.2	63.6	53.8	39.7	29.7
0.020	77.6	80.8	68.5	57.9	43.2

initial eccentricities of Umbriel ($e_2 \lesssim 0.005$), because the escape probability decreases for higher initial eccentricities of this satellite. In brief, in the frame of a planar model, we conclude that the eccentricity of Ariel plays a crucial role in the passage through the 5/3 MMR.

5. Complete secular dynamics

Adopting a secular circular model, Gomes and Correia (2023) have shown that non-zero inclinations of both satellites can also be important in the 5/3 MMR crossing. In addition, the currently observed inclinations are expected to correspond to the inclination values just after escaping the resonance (see Paper I), and can thus be used to put constraints on the pre-resonance configuration. Therefore, we now consider the complete secular problem presented in Sects. 2 and 3, that simultaneously takes into account non-zero eccentricities and non-zero inclinations.

The full secular problem has four degrees of freedom, and so it can only be accessed through numerical simulations and statistical analysis. In this section, we integrate the complete set of conservative differential equations (39) to (42) together with the complete set of dissipative tidal equations (54) to (61). We adopt exactly the same numerical setup from Sect. 4.5.1.

5.1. Resonance crossing

The exact location of the resonant islands is given by the resonant angles σ_k and φ_k (Eq. (14)), that is,

$$\dot{\sigma}_k \approx 5n_2 - 3n_1 - 2g_k = 0\,, \tag{87}$$

or

$$\dot{\varphi}_k \approx 5n_2 - 3n_1 - 2s_k = 0\,, \tag{88}$$

where $g_k \simeq d\varpi_k/dt$ and $s_k \simeq d\Omega_k/dt$ are the frequencies of the secular modes (see Sect. 2.3 in Paper I). The exact mean motion ratio for each resonance island is then given by

$$\frac{n_1}{n_2} = \frac{5}{3} - \frac{2}{3}\frac{g_k}{n_2}\,, \quad \text{or} \quad \frac{n_1}{n_2} = \frac{5}{3} - \frac{2}{3}\frac{s_k}{n_2}\,. \tag{89}$$

We have $g_1 > g_2 > s_2 > s_1$ for the satellites of Uranus (eg. Laskar, 1986, Paper I). Since $d/dt(n_1/n_2) < 0$, the system first encounters the inclination resonances at φ_k. Therefore, we initially expect some perturbation on the inclinations (Gomes and Correia, 2023), followed by some perturbations on the eccentricities (Sect. 4).

In Fig. 8, we provide four examples of the typical behaviours during the resonance crossing. Before the resonance encounter, the semi-major axes always follow the asymptotic evolution of an isolated two-body system (see Sect. 3.1 in Paper I), and the resonant arguments σ_k and φ_k circulate. In Fig. 8 a, we show an example of capture solely in the angles φ_k. At $t \approx 30$ Myr, the semi-major axes ratio locks with a value slightly higher than 5/3 and the resonance angles φ_k start to librate, while the angles σ_k continue to circulate. Just after the capture into resonance, the inclinations of both satellites grow steadily on average. In Fig. 8 b, we show an example of capture in the angles σ_k. Until $t \approx 40$ Myr, the evolution is similar to the one previously observed in Fig. 8 a, where capture in φ_k occurs at $t \approx 32$ Myr. However, at $t \approx 40$ Myr, the system quits the libration region, and the eccentricities and the inclinations start to evolve chaotically. After about 7 Myr in this regime, the resonant angles σ_k start to librate, while the angles φ_k circulate. From that point

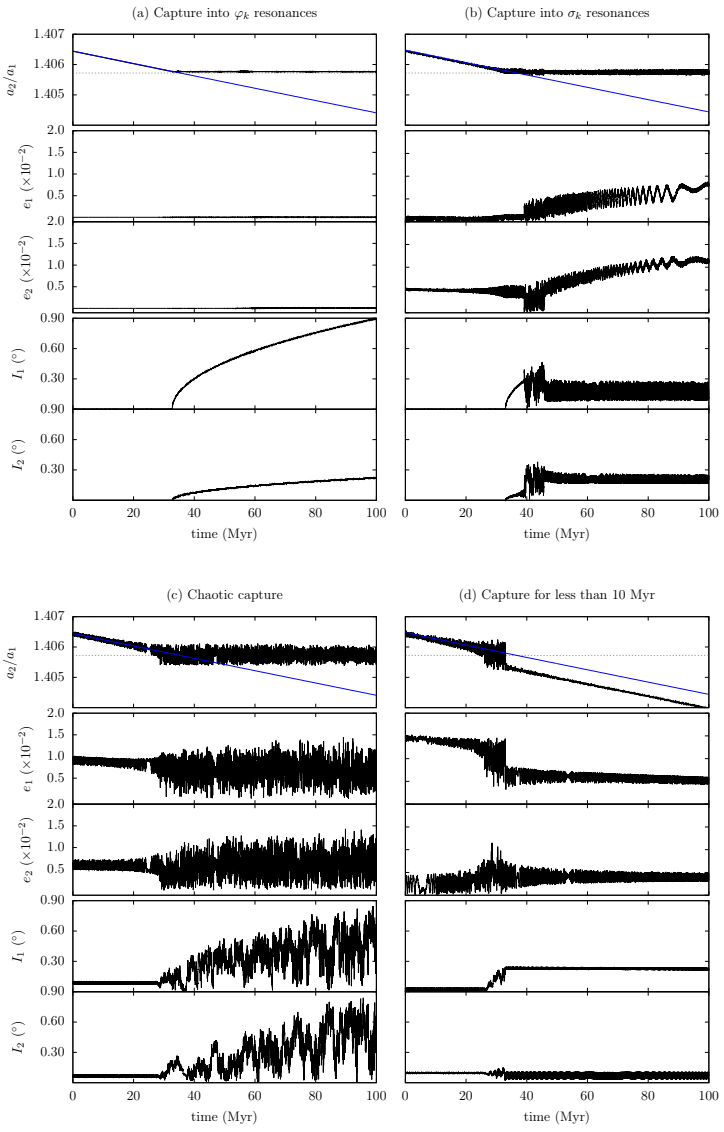

Figure 8: Four examples of a system crossing the 5/3 MMR with the secular model and initial $e_1 = e_2 = 10^{-5}$ and $I_1 = I_2 = 0.001°$ (a); $e_1 = 10^{-5}$, $e_2 = 5.0 \times 10^{-3}$ and $I_1 = I_2 = 0.001°$ (b); $e_1 = 10^{-2}$, $e_2 = 5.0 \times 10^{-3}$, $I_1 = 0.1°$, and $I_2 = 0.05°$ (c); $e_1 = 1.5 \times 10^{-2}$, $e_2 = 10^{-5}$, $I_1 = 0.001°$, and $I_2 = 0.10°$ (d). They correspond respectively to permanent capture in the resonant arguments φ_k (a), permanent capture in the resonant arguments σ_k (b), permanent capture in the chaotic region (c), and to a system that escapes the resonance in less than 10 Myr (d). From the top to the bottom, we show the semi-major axes ratio a_2/a_1; the eccentricities of Ariel and Umbriel, respectively; and the inclinations of Ariel and Umbriel, respectively. The blue line gives the asymptotic evolution (see Sect. 3.1 in Paper I), while the dashed line gives the position of the nominal resonance (Eq. (64)).

on, the eccentricities grow steadily on average, while the inclinations become constant on average. We also note that, between $t \approx 40$ Myr and 47 Myr, there is a slight decrease in the mean motion ratio constant value, resulting from the switch between the resonant arguments, from φ_k to σ_k (Eq. (89)). In Fig. 8 c, we show an example of permanent capture in the chaotic regime. The system is directly captured in the chaotic zone at $t \approx 32$ Myr. Then, the eccentricities and inclinations evolve chaotically and grow on average. Finally, in Fig. 8 d, we show an example of a short term capture inside the 5/3 MMR. The system is again directly captured in the chaotic region, which excites both eccentricities and inclinations, but manages to evade it in less than 10 Myr. After the resonance is crossed, the semi-major axes ratio returns to the predicted asymptotic evolution.

Table 3
Escape probability from the 5/3 MMR between Ariel-Umbriel for different initial eccentricities (e_1, e_2), combining all sets of initial inclination (I_1, I_2), computed from Table 5.

e_1 \ e_2	10^{-5}	0.005	0.010	0.015	0.020
10^{-5}	0.0	0.0	5.1	14.3	14.7
0.005	0.0	0.1	11.2	15.4	12.5
0.010	17.4	31.1	33.7	23.9	13.8
0.015	59.9	64.9	48.3	28.2	17.7
0.020	75.9	78.8	51.7	38.5	25.2

5.2. Escape probability

In order to get a global view of the possible outcomes of the resonance crossing, we explored a mesh of initial eccentricities ranging between 10^{-5} and 0.02, with a stepsize of 0.005, combined with a mesh of initial inclinations ranging between 0.001° and 0.2°, with a stepsize of 0.05°, totalling 625 different initial combinations of e_1, e_2, I_1, and I_2. For each initial combination, we performed 1 000 simulations for 100 Myr, evenly sampled over the resonant angle σ (Eq. (13)). For each run, we adopt the same numerical setup from Sect. 4.5.3, and determined that the system is captured in resonance if the semi-major axes ratio a_2/a_1 is still constant after 10 Myr inside the resonance as in the planar case (Sect. 4.5.3). In Appendix B (Table 5), we list the results that we obtained for the complete set of initial conditions.

We observe that for initial eccentricities smaller than about 0.005, long term capture is certain regardless of the initial inclinations. Actually, this very reduced dependency on the initial inclinations is observed throughout the whole mesh of initial conditions. That is, for the same pair of initial eccentricities (e_1, e_2), the escape probability is not very sensitive to changes in the initial pair of inclinations (I_1, I_2). Therefore, for a better analysis of the impact of the eccentricities on the escape probability of the 5/3 MMR, for each initial pair of (e_1,e_2), we can combine the results from the 25 combinations of initial pairs (I_1,I_2). The condensed results are shown in Table 3.

By comparing Table 2, obtained for the planar approximation (Sect. 4), with Table 3, obtained for the full eccentric and inclined problem, we observe that there is a good agreement between the two results, in particular for initial $e_2 \leq 0.005$. As in the planar approximation, the escape probability is more sensitive to variations in e_1 than in e_2. Furthermore, the escape probability is maximised for initial high values of e_1 and $e_2 \leq 0.005$ (about 80% of escapes). However, for initial $e_1 \geq 0.01$ and $e_2 > 0.005$, the escape probability decreases more significantly in the general case than in the planar approximation. Inversely, for initial $e_1 \leq 0.005$ and $e_2 > 0.005$, the escape probability is almost null in the planar case, while it becomes non-negligible and increases with e_2 in the general case.

5.3. Monte Carlo simulations

By adopting an initial discrete distribution on the eccentricities and inclinations, we were able to quantify the escape probability for each set of initial conditions. As a result, we have seen that the escape probability from the 5/3 MMR between Ariel and Umbriel is mostly dominated by the initial eccentricities and enhanced for initial $e_1 = 0.02$ and $e_2 \leq 0.005$. However, the final distribution of the inclinations is also very important, because it allows us to exclude all sets of initial conditions that fail to reproduce the current system (Gomes and Correia, 2023). Indeed, tidal dissipation is very inefficient to damp the inclinations (see Sect. 3.3 in Paper I), and so we expect that the inclination values (I_1,I_2) just after the resonance crossing match the currently observed mean values (Table 1).

The discrete nature of the distribution adopted in Sect. 5.2 may conceal some of the initial conditions that can reproduce the current configuration of the system. To ensure that all potential combinations of initial conditions are thoroughly examined, we employ the Monte Carlo method to encompass the entire range of initial combinations. We conducted one million simulations in which, for each run, we selected random initial eccentricities within the range of 0 and 0.02, random initial inclinations within the range of 0 and 0.2°, and random resonant angles σ_k and φ_k between 0° and 360°.

Overall, we find that 30% of the simulations successfully avoided capture. It is a non-negligible number, but it strongly depends on the initial conditions (Sect. 5.2). Therefore, we first look at the distribution of the initial eccentricities and initial inclinations that avoided capture into resonance. In Fig. 9, we divided the range of initial eccentricities $(0.00, 0.02)$ and initial inclinations $(0.00°, 0.2°)$ into a grid of 50×50 equally spaced intervals. We then

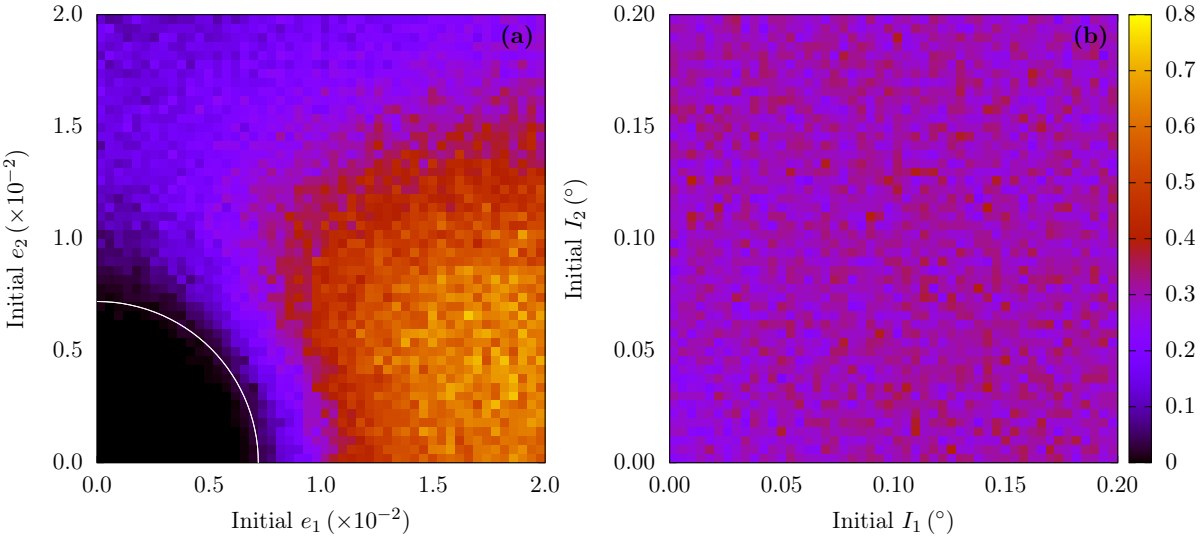

Figure 9: Escape probability from the 5/3 MMR between Ariel and Umbriel for a grid of 50×50 intervals, equally spaced between 0 and 0.02 for the initial eccentricities (a), and between 0 and 0.2° for the initial inclinations (b). The white circle corresponds to $\left(e_1^2 + e_2^2\right)^{1/2} = 0.0072$.

counted the number of initial conditions that escape capture in less than 10 Myr and divided by the total number of simulations in each bin. This provides a more in-depth examination of the escape probability distribution. Rather than relying on a fixed discrete set of initial conditions, we can now analyse a more continuous dataset, and pinpoint the values where behavioural changes occur in the initial conditions.

The analysis of the initial eccentricity distribution (Fig. 9 a), shows two distinct features: i) for initial $(e_1^2 + e_2^2)^{1/2} \lesssim 0.007$, all simulations were captured into resonance; ii) Ariel's high initial eccentricities facilitate the evasion, for initial $e_1 \gtrsim 0.01$ and $e_2 \lesssim 0.01$, the escape probability reaches $\sim$ 80%, whereas for the inverse case, that is, for initial $e_1 \lesssim 0.01$ and $e_2 \gtrsim 0.01$, the escape probability is around $\sim$ 30%. From the analysis of the initial inclinations distribution (Fig. 9 b), we observe a uniform spread across the phase space, devoid of any discernible trends, with escapes probabilities around $\sim$ 35%. We conclude that the results obtained with the Monte Carlo simulations are consistent with the results obtained with the discrete sampling (Sect. 5.2) and can thus be used for a deeper statistical analysis of the resonance crossing problem.

In Fig. 10, we show the distribution of the final eccentricities and final inclinations. We observe that both distributions are constrained within a cone[1], whose vertex is located at the origin of the distribution, that is, at $(e_1, e_2) = (0, 0)$ and $(I_1, I_2) = (0°, 0°)$, and widens as the values of eccentricity and inclination increase.

For the final eccentricity distribution (Fig. 10 a), we note that there is a denser concentration of points at the lower edge of the confinement cone, that is, for higher final e_1 and lower final e_2. In addition, there is a clear void of results for final eccentricities below 0.001. Both observations are related with the results shown in Fig. 9 a for the initial eccentricity distribution. Indeed, in order to escape capture, the initial eccentricity must be higher than ~ 0.007, and so it is more challenging to obtain near zero eccentricities after the system escapes the resonance. Similarly, the clustering of points in the region where $e_1 > e_2$ can be attributed to the higher probability of escape associated with higher initial eccentricity of Ariel ($e_1 > 0.01$) combined with lower initial eccentricity of Umbriel ($e_2 < 0.015$).

From the distribution of the final inclinations (Fig. 10 b), we can easily identify the simulations that closely match the presently observed mean values of I_1 and I_2 (Table 1). For that purpose, we established a circular region around the current mean values, with a radius of 0.002° (corresponding to $\sim$ 10% error in the current inclination of Ariel). These

[1]The exact shape corresponds to a hyperbolic conic section crossing the vertex of the cone, but for simplicity we refer to it as a cone.

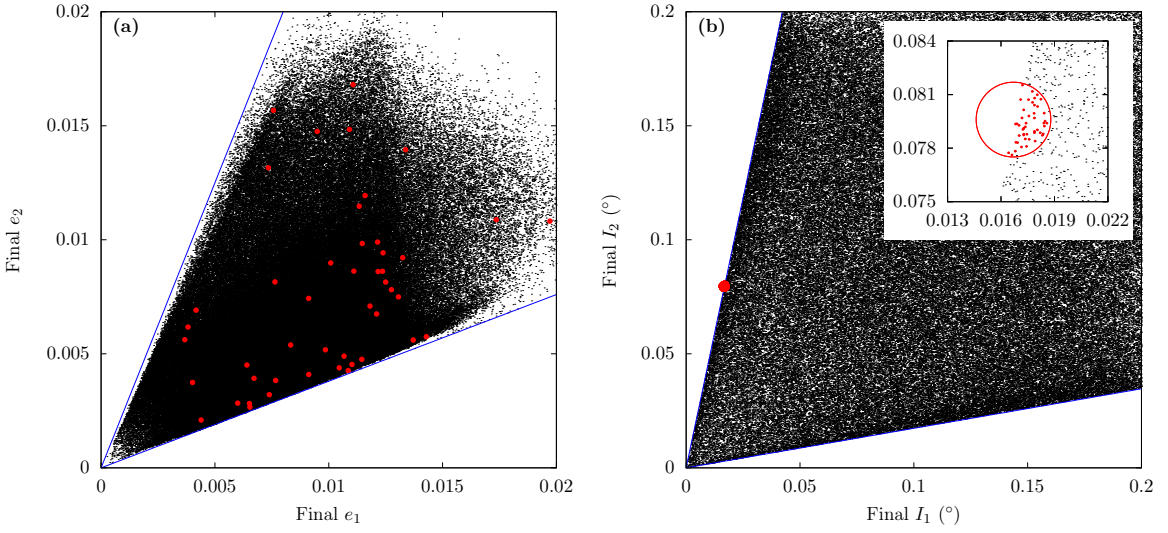

Figure 10: Distribution of the final eccentricities (a) and final inclinations (b) after the 5/3 MMR passage. The figures encompass 295 953 runs with random initial (e_1, e_2, I_1, I_2) that evade the resonance capture. From (b), we selected the points (in red) that lay inside a circle centred at the current mean inclinations of Ariel and Umbriel and a radius of 0.002° (Table 1).

points were coloured in red. We observe that the final eccentricities of these points are scattered across the confinement cone (Fig. 10 a), lacking any noticeable pattern.

Using solely the points that match the current mean inclinations (Table 1) after the 5/3 MMR passage, in Fig. 11, we show the distribution of the corresponding initial eccentricities and initial inclinations before the resonant encounter. For the distribution of the initial eccentricities (Fig. 11 a), we observe that the selected points are evenly distributed over the interval, provided that $e_1 > 0.005$. On the other hand, we observe that the initial inclinations of the selected points (Fig. 11 b) are well constrained within the interval $0.01° < I_1 < 0.05°$ and $0.06° < I_2 < 0.09°$. We hence conclude that this set of orbital elements prior to the resonant encounter best explains the currently observed system. We also remind that the final eccentricity values after the resonance passage are not important, because we expect tides to quickly damp them to the current values (see Sect. 3.2 in Paper I).

5.4. Final inclination distributions

In the previous section we have identified the most favourable initial conditions to cross the 5/3 MMR between Ariel and Umbriel. However, the resonance crossing is a stochastic process, and so identical initial conditions may lead to completely different evolutionary scenarios (Sect. 4.4).

The average initial inclination values that comply with the present system are given by $I_1 = 0.036°$ and $I_2 = 0.082°$ (Fig. 11 b). To investigate whether these initial inclinations can effectively replicate the present ones, we employed the same methodology used in Sect. 5.2. We fixed the initial (I_1, I_2) at the averaged values, and explored a mesh of initial eccentricities ranging between 10^{-5} and 0.02, with a step size of 0.005. For each set of initial (e_1, e_2), we ran 1 000 simulations for 100 Myr, equally distributed over the resonance angle σ, totalizing 25 000 simulations.

In Fig. 12, we show the histograms of the final inclinations distributed over 51 classes ranging between 0.0° and 0.3°, with a step size of 0.006°. We only considered the final inclinations from the simulations that escaped the 5/3 MMR, totalising 6 685 simulations. For each pair of initial (I_1, I_2), we combined the results from the 25 combinations of initial (e_1, e_2). The red dot gives the present mean inclinations of each body (Table 1). We observe that the histograms display prominent peaks for the final inclinations of Ariel and Umbriel around a well-defined mean value, which is close to the currently observed one.

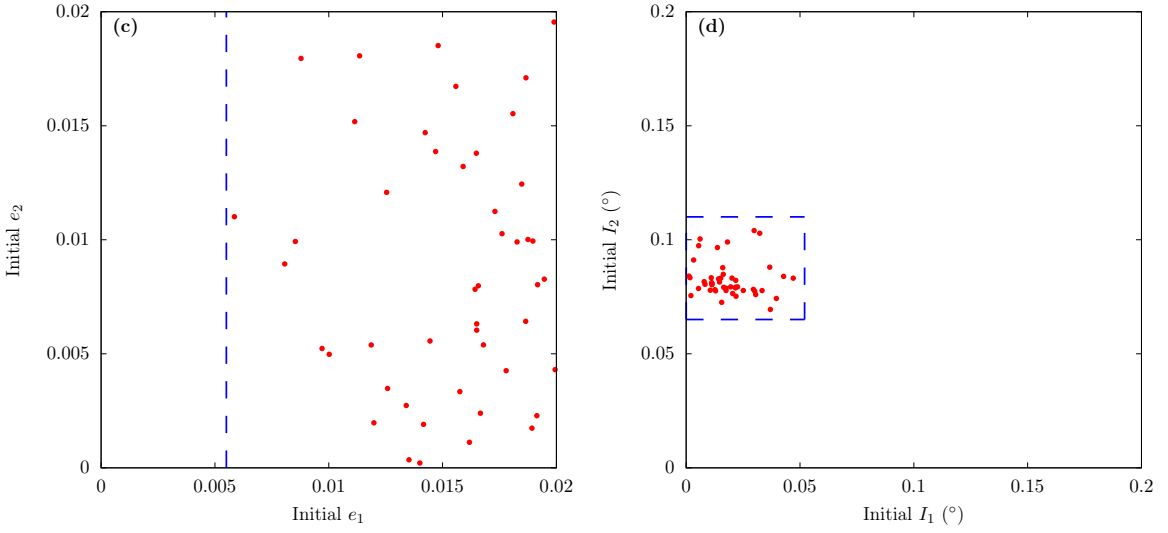

Figure 11: Distribution of the initial eccentricities (a) and initial inclinations (b) that reproduce the current mean inclinations (Table 1).

We repeated the experiment for other combinations of initial inclinations. To analyse the results systematically, we fitted a Lognormal point distribution function (PDF) to each histogram (with $x = I_k$),

$$f(x) = \frac{1}{x\,\eta\,\sqrt{2\pi}} \exp\left(-\frac{(\ln x - \upsilon)^2}{2\,\upsilon^2}\right), \tag{90}$$

where υ and η are the parameters that define the distribution. The peak of the PDF (mode), is given by

$$\langle x \rangle = \exp(\upsilon - \eta^2), \tag{91}$$

and the dispersion (variance) is given by

$$\Delta x = \left(\exp(\eta^2) - 1\right)\left(\exp(2\upsilon + \eta^2)\right) . \tag{92}$$

We observe that the observed mean inclination values are very close to the peak of the distribution and that the dispersion is very small. For the example shown in Fig. 12, we obtain $I_1 = 0.024° \pm 0.035°$ and $I_2 = 0.090° \pm 0.04°$, which compares with the observed mean values $I_1 = 0.017°$ and $I_2 = 0.080°$ (Table 1). We hence conclude that the initial conditions determined in Sect. 5.3 do correspond to reliable representations of the system prior to the resonance crossing.

6. $N-$body simulations

The results from the previous sections were obtained using a two-satellite secular model. In this section, we attempt to validate those results by adopting a more complete non-averaged $N-$body model. For that purpose, we use the numerical code `SPINS` (Correia, 2018), that takes into account satellite-satellite interactions, spin dynamics, rotational flattening, and tidal evolution according to the weak friction model. That is, it corresponds to the full non-averaged equations of motion that derive from the complete Hamiltonian given by Eq. (44). It is also the same numerical code that we used in Paper I.

6.1. Two-satellite simulations

We first compare the results of the secular model with the full three-body model (Uranus, Ariel, and Umbriel). This allows us to determine whether the secular model provides a good description of the system, or if the high-frequency terms, which were averaged out (Sect. 2.2.2), introduce some unexpected features. For a better comparison with the secular model simulations, we adopt here the exact same numerical setup from Sect. 4.5.1.

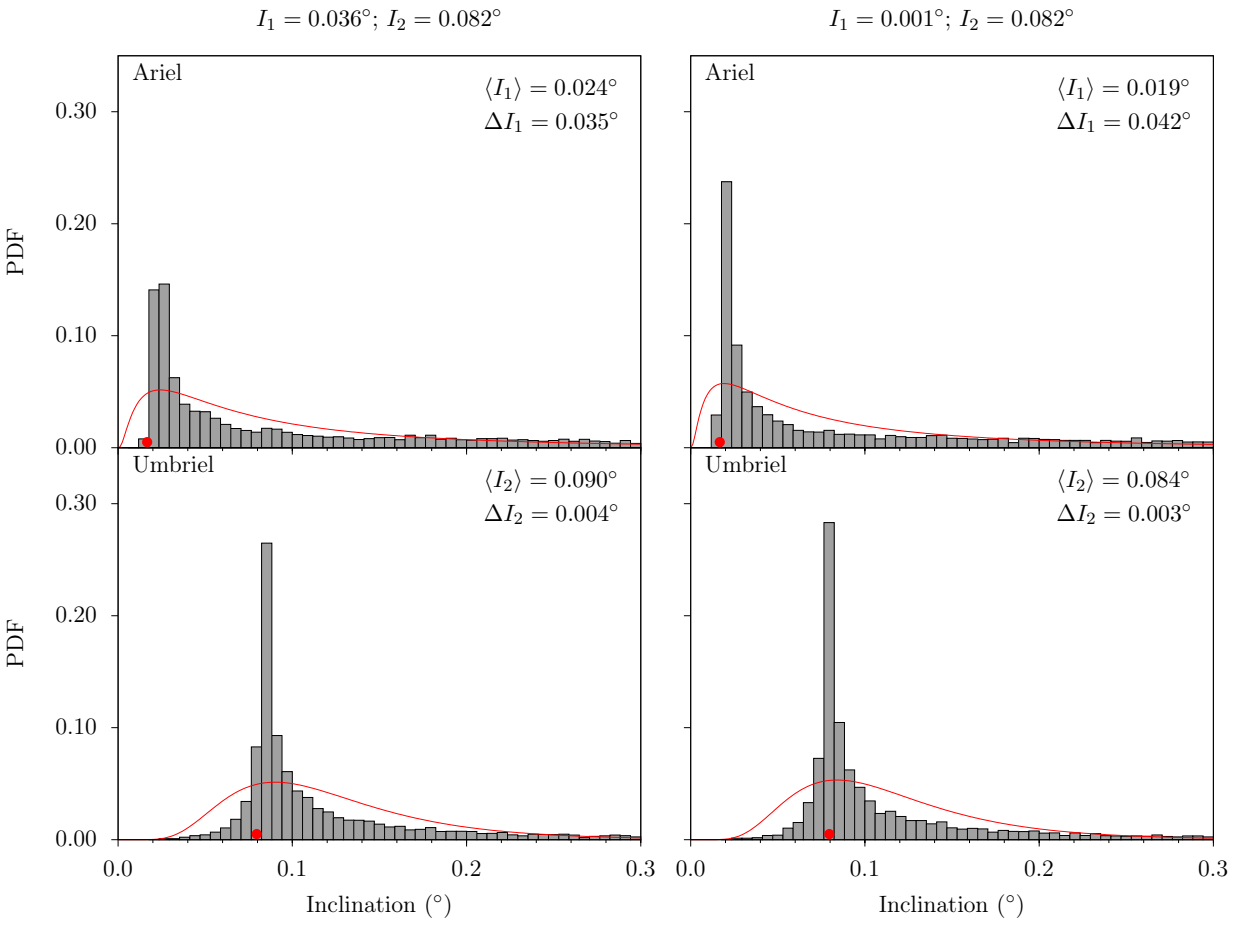

Figure 12: Histograms of the final inclination distributions of Ariel (top) and Umbriel (bottom) for initial inclinations $I_1 = 0.036°$ and $I_2 = 0.082°$. We show the best fit Lognormal distribution (Eq. (90)) to each histogram (red curve) and the corresponding inclination mode, $\langle I \rangle$, and variance, ΔI. The presently observed inclinations (Table 1) are marked with red dots.

In a first experiment, we aim to verify the low impact of the initial inclinations. We then fix the initial $I_1 = 0.001°$, and vary I_2 between $0.001°$ and $0.20°$, with a step size of $0.05°$. To simultaneously check the role of the initial eccentricity of Ariel into the capture probability, we fix the initial $e_2 = 10^{-5}$ and vary e_1 between 10^{-5} and 0.02, with a step size of 0.005. This totalises 25 initial combinations of (e_1, I_2).

The computation time to integrate these initial conditions for 100 Myr with the three-body model is 10^4 longer than with the secular model. Therefore, it is not feasibly to compute 1 000 runs equally distributed over the resonance angle σ for every pair of initial (e_1, I_2). We thus reduced the number of simulations per initial condition by a factor of ten, to 100 runs for each pair, which gives a total number of 2 500 simulations. Then, for each run, we determine again if the system evades the 5/3 MMR between Ariel and Umbriel in less than 10 Myr by evaluating the semi-major axes ratio a_2/a_1 (see Sect. 4.5.3).

In Table 4, we show the escape probability for the 25 pairs of initial (e_1, I_2) obtained with the three-body model. For a better comparison, we also show the results obtained with the secular model[2]. For $e_1 \leq 0.005$, both models show that capture in resonance is certain, independently of the initial I_2. For $e_1 \geq 0.01$, we observe that the escape probabilities obtained with the two models are in good agreement, despite some small local variations which are most likely due to statistical fluctuations. In particular, we confirm that outside the secular approximation, there is not much

[2]The results from the secular model were obtained in Sect. 5.2 and displayed here again for a more convenient comparison between the two sets of results (see also Table 5).

Table 4
Escape probability from the 5/3 MMR between Ariel and Umbriel for a mesh of 25 initial pairs of (e_1, I_2), with $e_2 = 10^{-5}$ and $I_1 = 0.001°$, obtained with three different numerical models.

Secular model (Sect. 5.2)

I_2 \ e_1	10^{-5}	0.005	0.010	0.015	0.020
0.001°	0	0	22	49	60
0.05°	0	0	21	55	66
0.10°	0	0	19	61	72
0.15°	0	0	18	63	74
0.20°	0	0	20	59	74

Two-satellite model (Sect. 6.1)

I_2 \ e_1	10^{-5}	0.005	0.010	0.015	0.020
0.001°	0	0	37	46	59
0.05°	0	0	37	54	48
0.10°	0	0	27	55	54
0.15°	0	0	16	62	56
0.20°	0	0	36	67	48

Five-satellite model (Sect. 6.2)

I_2 \ e_1	10^{-5}	0.005	0.010	0.015	0.020
0.001°	0	0	4	62	82
0.05°	0	0	13	72	77
0.10°	0	0	7	67	85
0.15°	0	0	15	70	86
0.20°	0	0	10	65	90

impact from the inclination of Umbriel and the initial eccentricity of Ariel remains the key parameter that controls the escape probability.

According to the secular model (Sect. 5.3), the currently observed system (Table 1) can be replicated with initial inclinations $(I_1, I_2) = (0.001°, 0.082°)$. To ensure a low capture probability in resonance, we chose initial $(e_1, e_2) = (0.015, 0.005)$. With these initial eccentricity and inclination values, we then integrated one set of 100 simulations evenly distributed across σ for 100 Myr using the secular model and another set of 100 simulations using the three-body model.

In Fig. 13, we built a histogram of the final eccentricity and inclination distributions. For a better comparison, we overlaid the Lognormal curve obtained with the secular model (Eq. (90)). We observe that the Lognormal curve presents a remarkable adjustment to the results obtained with the three-body model. For the final eccentricities, the differences can be likely attributed to statistical fluctuations. For the final inclinations, the distributions also display the same diffusion pattern, although the secular model exhibits a more pronounced peak. The good agreement observed between the two models demonstrates that the secular model provides a correct description of the two-satellite system composed by Ariel and Umbriel.

6.2. Five-satellite simulations

For simplicity, up to now we have studied the 5/3 MMR passage between Ariel and Umbriel by building models that consider only these two satellites. However, mutual gravitational interactions with the remaining satellites of Uranus may also influence the architecture of the entire system during the resonance passage (Ćuk et al., 2020). Therefore, in this section we compare the previous results with the full six-body model (Uranus, Miranda, Ariel, Umbriel, Titania, and Oberon).

The physical properties of the satellites are given in Table 1. For the Love numbers of Miranda, Titania, and Oberon, we adopt $k_{2,M} = 8.84 \times 10^{-4}$, $k_{2,T} = 1.99 \times 10^{-2}$, and $k_{2,O} = 1.68 \times 10^{-2}$ (Chen et al., 2014), together with $\tau_M = 38.9$ s, $\tau_T = 239.4$ s, and $\tau_O = 370.2$ s (corresponding to $Q_k = 500$, see Sect. 3.2 in Paper I for details), yielding

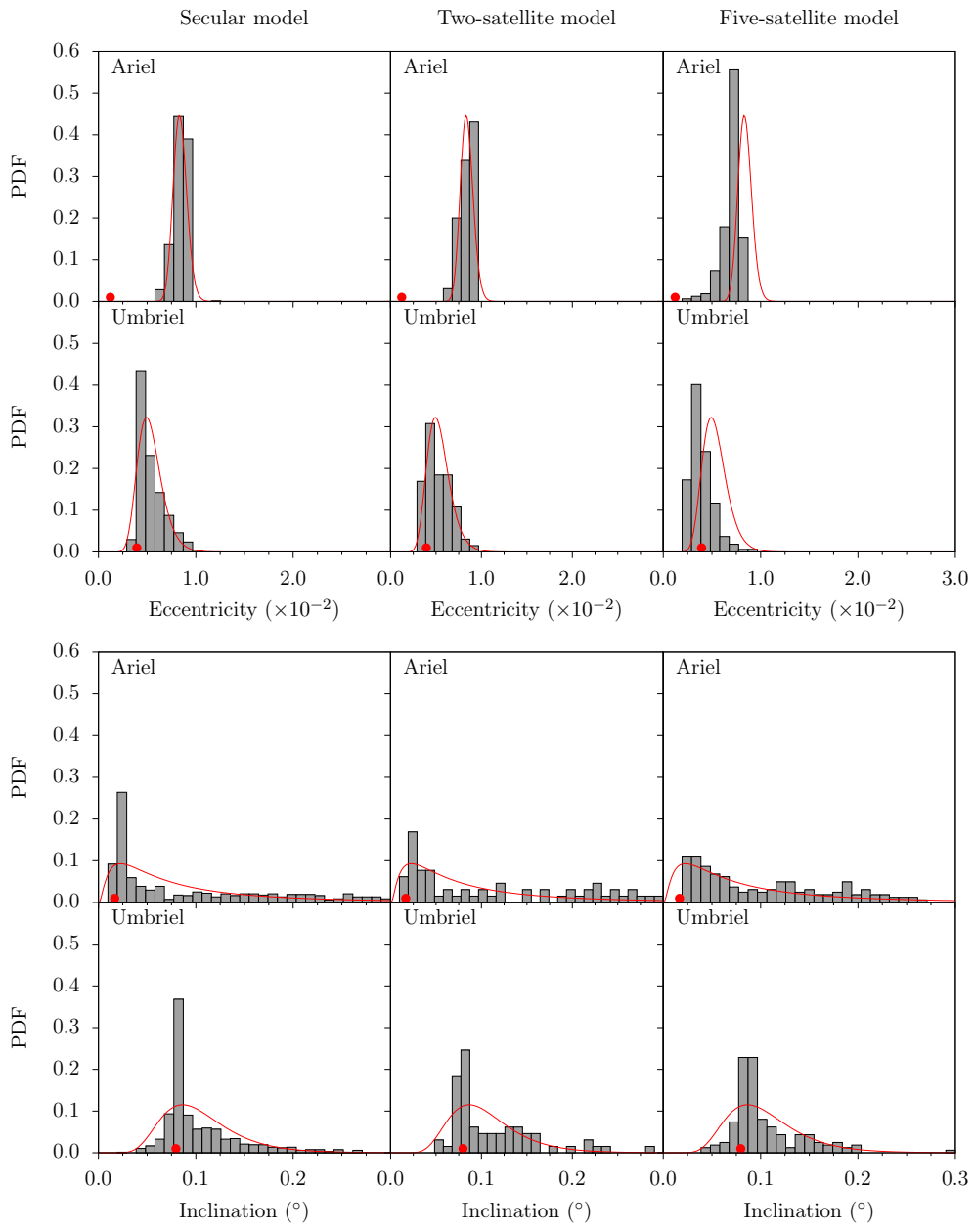

Figure 13: Histograms of the final eccentricity and inclination distributions of Ariel (top) and Umbriel (bottom) for initial $e_1 = 0.015$, $e_2 = 0.005$, $I_1 = 0.001°$, and $I_2 = 0.082°$. We show the results for the secular model (left), the two-satellite model (middle), and the five-satellite model (right). We also show the best fit Lognormal distribution (Eq. (90)) to the histogram of the secular model (red curve). The presently observed inclinations (Table 1) are marked with red dots.

to

$$k_{2,M}\,\tau_M = 0.034\,\mathrm{s}\,, \quad k_{2,T}\,\tau_T = 4.764\,\mathrm{s}\,, \quad \text{and} \quad k_{2,O}\,\tau_O = 6.219\,\mathrm{s}\,. \tag{93}$$

The total angular momentum of the system also needs to be updated (Eq. (83)) to accommodate the five satellites,

$$\Sigma = 9.446\,072 \times 10^{-10}\ \mathrm{M}_\odot\,\mathrm{au}^2\,\mathrm{yr}^{-1}\,. \tag{94}$$

The semi-major axes of the satellites at the nominal resonance were again calculated as for the two-satellite case (Eq. (64)). The angular velocity of Uranus is corrected according to Eq. (84), such that the current total angular momentum of the system is conserved (Eq. (94)). Finally, the semi-major axis of Ariel is slightly decreased to move the system from the nominal resonance, leading to

$$\begin{aligned} a_M/R_0 &= 5.0794\,, \\ a_A/R_0 &= 7.3868\,, \\ a_U/R_0 &= 10.3891\,, \\ a_T/R_0 &= 17.0671\,, \\ a_O/R_0 &= 22.8239\,. \end{aligned} \tag{95}$$

We first attempted to reproduce the results in Table 4. We fixed $e_2 = 10^{-5}$ and $I_1 = 0.001°$ and integrated the whole system over 100 Myr for different initial (e_1, I_2) pairs. For each pair, we ran 100 simulations equally distributed over σ. The initial eccentricities and inclinations for Miranda, Titania, and Oberon were kept at the currently observed values (Table 1). For each simulation, we again checked if the system evades the 5/3 MMR between Ariel and Umbriel in less than 10 Myr. When we increase the number of bodies in the system, the computation time increases even more. The five-satellite simulations are about four times longer than the two-satellite simulations (Sect. 6.1).

By comparing the results between the different models, we verify again that for $e_1 \leq 0.01$, it is never possible to escape the 5/3 MMR. We also confirm that the initial inclination of Umbriel does not play any significant role. However, some minor differences can be observed with respect to the secular and two-satellite models. In general, for $e_1 = 0.015$, the five-satellite model provides lower escape probabilities. On the other hand, for $e_1 \geq 0.015$, it provides higher escape probabilities. That is, it appears that the perturbations from the remaining satellites initially difficult the resonance crossing, but after some critical value $e_1 \sim 0.01$, these perturbations facilitate the evasion.

In a second experiment, we integrated a set of 100 simulations equally distributed over σ with the best suited initial eccentricities and inclinations of Ariel and Umbriel that are able to reproduce the current system (Table 1). The initial eccentricities and inclinations for Miranda, Titania, and Oberon were kept at the currently observed values, but for Ariel and Umbriel we adopted $e_1 = 0.015$, $I_1 = 0.001°$, $e_2 = 0.005$, and $I_2 = 0.082°$, respectively, as in Sect. 6.1.

In Fig. 13, we built a histogram of the final eccentricity and inclination distributions. For a better comparison with the previous models, we overlaid the Lognormal curve obtained with the secular model (Eq. (90)). We observe that there is still a good agreement between the five-satellite model and the secular and two-satellite models. This is particularly true for the inclination distributions, whose differences with respect to the two-satellite are mostly likely due to statistical fluctuations. Concerning the eccentricity distributions, there is a slight shift of the peak of maximal eccentricity to lower values. However, this discrepancy is not really a problem, because in the case of Umbriel this peak is still very close to the currently observed mean value, while in the case of Ariel, any remnant eccentricity is expected to be quickly damped to the currently observed value (see Sect. 3.2 in Paper I).

In Fig. 14, we plot one example of the 100 simulations with the five-satellite model, where the system skips the 5/3 MMR between Ariel and Umbriel. We show the evolution of the semi-major axes, eccentricities, inclinations, and obliquities of all satellites. Prior to the commensurability, the average semi-major axes follow the asymptotic tidal evolution (blue line), while the eccentricities and inclinations oscillate around a mean value close to the initial ones. As the system crosses the nominal resonance, the semi-major axes of Ariel and Umbriel quickly shift, placing the mean-motion ratio below the nominal resonance, and thus avoiding entrapment in resonance. Simultaneously, the eccentricity of Ariel quickly drops, while the eccentricity of Miranda grows. The eccentricity of Umbriel, Titania, and Oberon, as well as the inclinations of all the satellites, appear to be unaffected by the resonance crossing. The subsequent tidal damping on the eccentricity of Miranda and Ariel is expected to drive the system close to the present state after 640 Myr (see Sect. 4 in Paper I). This example thus confirms that it is possible to cross the 5/3 MMR between Ariel and Umbriel and recover the currently observed system (Table 1), as long as the initial eccentricity of Ariel before the resonance is $e_1 \geq 0.015$. It also shows that the obliquities of all satellites settle into the low obliquity Cassini state 1 (see Paper I) instead of developing high obliquities (Ćuk et al., 2020).

Furthermore, in simulations where the system was captured for an extended period of time, we observed a significant increase in both the eccentricity and inclination values of Miranda. This aligns with the findings of Ćuk et al. (2020), supporting that, despite not being directly involved in the resonance, due to its relatively small mass, Miranda's orbit is severely affected by a lengthening passage through the 5/3 MMR between Ariel and Umbriel.

7. Conclusion

The Uranian satellites Ariel and Umbriel have most likely passed through the 5/3 MMR in the past owing to the tidal evolution of their orbits. In this paper, we have revisited the crossing of this resonance to ascertain the initial conditions that allow the system to evade capture and evolve into the present configuration.

To address this issue, we developed a secular resonant two-satellite model with low eccentricities and low inclinations, using a Hamiltonian approach similar to Tittemore and Wisdom (1990). However, in our model we introduced the spin evolution of the planet and the satellites, and we adopted the total angular momentum of the system as a canonical variable, which is conserved and naturally removes one degree of freedom from the problem. We also developed a Hamiltonian extension to include tides based on the weak friction constant time-lag model (eg. Mignard, 1979), which provides the complete tidal evolution for all variables in the problem.

By applying our model to Ariel and Umbriel, we numerically studied in detail the passage through the 5/3 MMR between the two satellites. At first, we revisited the problem in the planar approximation to better compare with previous studies. The crossing of the 5/3 MMR is a stochastic process, and so we performed a large number of numerical simulations covering many different combinations for the initial eccentricities of Ariel and Umbriel. We observed that the eccentricity of at least one of the satellites must be higher than 0.007 in order to avoid capture in resonance. However, we have shown that a high eccentricity of Ariel translates into an increased likelihood of evading the 5/3 MMR.

We then considered the effects of both eccentricity and inclination in the resonance passage. Once more, we performed a large number of numerical simulations across a mesh of discrete combinations of initial conditions. We observed that the inclinations do not impact significantly the escape probability and retrieved similar results as in the planar approximation case.

The discrete nature of the previous analysis compelled us to adopt a Monte Carlo methodology, and perform one million simulations with random initial eccentricities, inclinations, and longitudes. These results have shown that the optimal configuration to enhance the escape probability is achieved when the initial eccentricities are $e_1 \geq 0.01$ and $e_2 \leq 0.015$. Following the resonance passage, the eccentricities are usually higher than the currently observed ones (Table 1), but they can be quickly eroded owing to tidal damping, in particular for Ariel. The Monte Carlo method also allowed us to constrain the initial inclinations of the system, we expect that $I_1 \leq 0.05°$ and $I_2 \approx 0.08°$, so that the final inclinations after the resonance passage match the current inclinations of the system (Table 1).

Finally, the results obtained with the secular model were inspected using a complete $N-$body model with two and five-satellites. We did not observe any significant differences between the three models, which confirms that the long-term evolution through the 5/3 MMR is mainly driven by the secular interactions between Ariel and Umbriel. Therefore, the results regarding Ariel and Umbriel obtained with the secular model are still valid for the complete, five-satellite case. We also observed that the orbits of Titania and Oberon do not show any perceptive modifications when the resonance is shortly skipped. However, as in Ćuk et al. (2020), we realize that the orbit of Miranda can be severely excited during the resonance entrapment, increasing both the eccentricity and inclination. In addiction, the final eccentricity and inclination values observed with the five-satellite simulations closely match with the values estimated in Paper I as necessary to replicate the current architecture of the system (Gomes and Correia, 2024a).

To accomplish the relatively high initial eccentricity of Ariel and inclination of Umbriel, some past dynamical events must have occurred that excited both values. Since tides are very inefficient to damp the inclination, Umbriel's value can be attributed to the possible passage through the past 3/1 MMR between Miranda and Umbriel (Tittemore and Wisdom, 1989). As for the Ariel's initial eccentricity, the strong eccentricity damping requires that the excitation must have occurred shortly before the encounter with the 5/3 MMR. The best candidates are the third order 7/4 MMR resonance between Ariel and Umbriel (see Fig. 1 in Paper I) or some first order three-body MMR, which can also excite the eccentricity (eg. Petit, 2021). Therefore, future work on the past dynamical evolution of the Uranian satellite system should try to address this point.

Acknowledgements

This work was supported by COMPETE 2020 and by FCT - Fundação para a Ciência e a Tecnologia, I.P., Portugal, through the projects SFRH/BD/143371/2019, GRAVITY (PTDC/FIS-AST/7002/2020), ENGAGE SKA (POCI-01-0145-FEDER-022217), and CFisUC (UIDB/04564/2020 and UIDP/04564/2020, with DOI identifiers 10.54499/UIDB/04564/2020 and 10.54499/UIDP/04564/2020, respectively). We acknowledge the Laboratory for Advanced Computing at University of Coimbra (https://www.uc.pt/lca) for providing the resources to perform the numerical simulations.

References

Alexander, M.E., 1973. The Weak Friction Approximation and Tidal Evolution in Close Binary Systems. Astrophysics and Space Science 23, 459–510. doi:10.1007/BF00645172.

Avramchuk, V.V., Rosenbush, V.K., Bul'Ba, T.P., 2007. Photometric study of the major satellites of Uranus. Solar System Research 41, 186–202. doi:10.1134/S0038094607030021.

Cartwright, R.J., Beddingfield, C.B., Nordheim, T.A., Roser, J., Grundy, W.M., Hand, K.P., Emery, J.P., Cruikshank, D.P., Scipioni, F., 2020. Evidence for Ammonia-bearing Species on the Uranian Satellite Ariel Supports Recent Geologic Activity. The Astrophysical Journal Letters 898, L22. doi:10.3847/2041-8213/aba27f, arXiv:2007.02826.

Castillo-Rogez, J., Weiss, B., Beddingfield, C., Biersteker, J., Cartwright, R., Goode, A., Melwani Daswani, M., Neveu, M., 2023. Compositions and interior structures of the large moons of uranus and implications for future spacecraft observations. Journal of Geophysical Research: Planets 128, e2022JE007432. URL: https://agupubs.onlinelibrary.wiley.com/doi/abs/10.1029/2022JE007432, doi:https://doi.org/10.1029/2022JE007432, arXiv:https://agupubs.onlinelibrary.wiley.com/doi/pdf/10.1029/2022JE007432. e2022JE007432 2022JE007432.

Chen, E.M.A., Nimmo, F., Glatzmaier, G.A., 2014. Tidal heating in icy satellite oceans. Icarus 229, 11–30. doi:10.1016/j.icarus.2013.10.024.

Correia, A.C.M., 2018. Chaotic dynamics in the (47171) Lempo triple system. Icarus 305, 250–261. doi:10.1016/j.icarus.2018.01.008, arXiv:1710.08401.

Correia, A.C.M., Rodríguez, A., 2013. On the Equilibrium Figure of Close-in Planets and Satellites. The Astrophysical Journal 767, 128. doi:10.1088/0004-637X/767/2/128, arXiv:1304.1425.

Couetdic, J., Laskar, J., Correia, A.C.M., Mayor, M., Udry, S., 2010. Dynamical stability analysis of the HD 202206 system and constraints to the planetary orbits. Astronomy and Astrophysics 519, A10. doi:10.1051/0004-6361/200913635, arXiv:0911.1963.

Ćuk, M., El Moutamid, M., Tiscareno, M.S., 2020. Dynamical History of the Uranian System. Plan. Sci. J. 1, 22. doi:10.3847/PSJ/ab9748, arXiv:2005.12887.

Darwin, G.H., 1880. On the Secular Changes in the Elements of the Orbit of a Satellite Revolving about a Tidally Distorted Planet. Philos. Trans. R. Soc. London 171, 713–891.

Delisle, J.B., Laskar, J., Correia, A.C.M., Boué, G., 2012. Dissipation in planar resonant planetary systems. Astronomy and Astrophysics 546, A71. doi:10.1051/0004-6361/201220001, arXiv:1207.3171.

Dermott, S.F., Nicholson, P.D., 1986. Masses of the satellites of Uranus. Nature 319, 115–120. doi:10.1038/319115a0.

Dumas, H.S., Laskar, J., 1993. Global dynamics and long-time stability in Hamiltonian systems via numerical frequency analysis. Physical Review Letters 70, 2975–2979. doi:10.1103/PhysRevLett.70.2975.

Gastineau, M., Laskar, J., 2011. Trip: A computer algebra system dedicated to celestial mechanics and perturbation series. ACM Commun. Comput. Algebra 44, 194–197. URL: http://doi.acm.org/10.1145/1940475.1940518, doi:10.1145/1940475.1940518.

Gavrilov, S.V., Zharkov, V.N., 1977. Love Numbers of the Giant Planets. Icarus 32, 443–449. doi:10.1016/0019-1035(77)90015-X.

Goldstein, H., 1950. Classical mechanics. Addison-Wesley, Reading.

Gomes, S.R.A., Correia, A.C.M., 2023. Effect of the inclination in the passage through the 5/3 mean motion resonance between Ariel and Umbriel. Astronomy and Astrophysics 674, A111. doi:10.1051/0004-6361/202346101, arXiv:2305.08794.

Gomes, S.R.A., Correia, A.C.M., 2024a. Dynamical evolution of the Uranian satellite system I. From the 5/3 Ariel–Umbriel mean motion resonance to the present. arXiv e-prints .

Gomes, S.R.A., Correia, A.C.M., 2024b. Stability maps for the 5/3 mean motion resonance between Ariel and Umbriel with inclination. arXiv e-prints , arXiv:2309.04786doi:10.48550/arXiv.2309.04786, arXiv:2309.04786.

Greenberg, R., 1975. The Dynamics of Uranus' Satellites. Icarus 24, 325–332. doi:10.1016/0019-1035(75)90128-1.

Ida, S., Ueta, S., Sasaki, T., Ishizawa, Y., 2020. Uranian satellite formation by evolution of a water vapour disk generated by a giant impact. Nature Astronomy 4, 880–885. doi:10.1038/s41550-020-1049-8, arXiv:2003.13582.

Inderbitzi, C., Szulágyi, J., Cilibrasi, M., Mayer, L., 2020. Formation of satellites in circumplanetary discs generated by disc instability. Monthly Notices of the Royal Astronomical Society] 499, 1023–1036. doi:10.1093/mnras/staa2796, arXiv:1912.11406.

Ishizawa, Y., Sasaki, T., Hosono, N., 2019. Can the Uranian Satellites Form from a Debris Disk Generated by a Giant Impact? The Astrophysical Journal 885, 132. doi:10.3847/1538-4357/ab48ef, arXiv:1909.13065.

Jacobson, R.A., 2014. The Orbits of the Uranian Satellites and Rings, the Gravity Field of the Uranian System, and the Orientation of the Pole of Uranus. The Astronomical Journal 148, 76. doi:10.1088/0004-6256/148/5/76.

Kaula, W.M., 1964. Tidal dissipation by solid friction and the resulting orbital evolution. Rev. Geophys. 2, 661–685.

Lambeck, K., 1980. The Earth's Variable Rotation: Geophysical Causes and Consequences. Cambridge University Press.

Laskar, J., 1986. A general theory for the Uranian satellites. Astronomy and Astrophysics 166, 349–358.

Laskar, J., 1990. The chaotic motion of the solar system - A numerical estimate of the size of the chaotic zones. Icarus 88, 266–291. doi:10.1016/0019-1035(90)90084-M.

Laskar, J., 1993. Frequency analysis for multi-dimensional systems. Global dynamics and diffusion. Physica D Nonlinear Phenomena 67, 257–281. doi:10.1016/0167-2789(93)90210-R.

Malhotra, R., Dermott, S.F., 1990. The role of secondary resonances in the orbital history of Miranda. Icarus 85, 444–480. doi:10.1016/0019-1035(90)90126-T.

Mignard, F., 1979. The evolution of the lunar orbit revisited. I. Moon and Planets 20, 301–315.

Murray, C.D., Dermott, S.F., 2000. Solar system dynamics. Cambridge University Press. doi:10.1017/CBO9781139174817.

Peale, S.J., 1988. Speculative histories of the Uranian satellite system. Icarus 74, 153–171. doi:10.1016/0019-1035(88)90037-1.

Petit, A.C., 2021. An integrable model for first-order three-planet mean motion resonances. Celestial Mechanics and Dynamical Astronomy 133, 39. doi:10.1007/s10569-021-10035-7, arXiv:2107.06299.

Plescia, J.B., 1987. Cratering history of the Uranian satellites: Umbriel, Titania, and Oberon. Journal of Geophysical Research 92, 14918–14932. doi:10.1029/JA092iA13p14918.

Pollack, J.B., Lunine, J.I., Tittemore, W.C., 1991. Origin of the Uranian satellites., in: Bergstralh, J.T., Miner, E.D., Matthews, M.S. (Eds.), Uranus, pp. 469–512.

Rufu, R., Canup, R.M., 2022. Coaccretion + Giant-impact Origin of the Uranus System: Tilting Impact. The Astrophysical Journal 928, 123. doi:10.3847/1538-4357/ac525a, arXiv:2204.00124.

Singer, S.F., 1968. The Origin of the Moon and Geophysical Consequences. Geophys. J. R. Astron. Soc. 15, 205–226.

Smart, W.M., 1953. Celestial Mechanics. London, New York, Longmans, Green.

Smith, B.A., Soderblom, L.A., Beebe, R., Bliss, D., Boyce, J.M., Brahic, A., Briggs, G.A., Brown, R.H., Collins, S.A., Cook, A.F., Croft, S.K., Cuzzi, J.N., Danielson, G.E., Davies, M.E., Dowling, T.E., Godfrey, D., Hansen, C.J., Harris, C., Hunt, G.E., Ingersoll, A.P., Johnson, T.V., Krauss, R.J., Masursky, H., Morrison, D., Owen, T., Plescia, J.B., Pollack, J.B., Porco, C.C., Rages, K., Sagan, C., Shoemaker, E.M., Sromovsky, L.A., Stoker, C., Strom, R.G., Suomi, V.E., Synnott, S.P., Terrile, R.J., Thomas, P., Thompson, W.R., Veverka, J., 1986. Voyager 2 in the Uranian System: Imaging Science Results. Science 233, 43–64. doi:10.1126/science.233.4759.43.

Squyres, S.W., Reynolds, R.T., Lissauer, J.J., 1985. The enigma of the Uranian satellites' orbital eccentricities. Icarus 61, 218–223. doi:10.1016/0019-1035(85)90103-4.

Strom, R.G., 1987. The solar system cratering record: Voyager 2 results at Uranus and implications for the origin of impacting objects. Icarus 70, 517–535. doi:10.1016/0019-1035(87)90093-5.

Szulágyi, J., Cilibrasi, M., Mayer, L., 2018. In Situ Formation of Icy Moons of Uranus and Neptune. The Astrophysical Journal Letters 868, L13. doi:10.3847/2041-8213/aaeed6, arXiv:1811.06574.

Thomas, P.C., 1988. Radii, shapes, and topography of the satellites of Uranus from limb coordinates. Icarus 73, 427–441. doi:10.1016/0019-1035(88)90054-1.

Tittemore, W.C., Wisdom, J., 1988. Tidal evolution of the Uranian satellites I. Passage of Ariel and Umbriel through the 5:3 mean-motion commensurability. Icarus 74, 172–230. doi:10.1016/0019-1035(88)90038-3.

Tittemore, W.C., Wisdom, J., 1989. Tidal evolution of the Uranian satellites II. An explanation of the anomalously high orbital inclination of Miranda. Icarus 78, 63–89. doi:10.1016/0019-1035(89)90070-5.

Tittemore, W.C., Wisdom, J., 1990. Tidal evolution of the Uranian satellites III. Evolution through the Miranda-Umbriel 3:1, Miranda-Ariel 5:3, and Ariel-Umbriel 2:1 mean-motion commensurabilities. Icarus 85, 394–443. doi:10.1016/0019-1035(90)90125-S.

Verheylewegen, E., Noyelles, B., Lemaitre, A., 2013. A numerical exploration of Miranda's dynamical history. Monthly Notices of the Royal Astronomical Society] 435, 1776–1787. doi:10.1093/mnras/stt1415, arXiv:1302.4329.

Zahnle, K., Schenk, P., Levison, H., Dones, L., 2003. Cratering rates in the outer Solar System. Icarus 163, 263–289. doi:10.1016/S0019-1035(03)00048-4.

A. Conservative Hamiltonian terms

We note that,

$$\mathcal{K}_1 = -\frac{p}{2}\frac{\mu_1^2\beta_1^3}{\Gamma_1^3} + \left(1+\frac{p}{2}\right)\frac{\mu_2^2\beta_2^3}{\Gamma_2^3}\,, \tag{96}$$

$$\mathcal{K}_2 = -\frac{3}{2}\left(\frac{p^2}{4}\frac{\mu_1^2\beta_1^3}{\Gamma_1^4} + \left(1+\frac{p}{2}\right)^2\frac{\mu_2^2\beta_2^3}{\Gamma_2^4}\right)\,, \tag{97}$$

$$\mathcal{O}_1 = \frac{3}{2}J_2R^2\left(-\frac{(2p+q)}{q}\frac{\mu_1^4\beta_1^7}{\Gamma_1^7} + \frac{2(p+q)}{q}\frac{\mu_2^4\beta_2^7}{\Gamma_2^7}\right)\,, \tag{98}$$

$$\mathcal{O}_2 = \frac{3}{2}J_2R^2\left(-\frac{2p}{q}\frac{\mu_1^4\beta_1^7}{\Gamma_1^7} + \frac{(2p+q)}{q}\frac{\mu_2^4\beta_2^7}{\Gamma_2^7}\right)\,, \tag{99}$$

$$\mathcal{O}_3 = \frac{3}{2}J_2R^2\left(-(p-1)\frac{\mu_1^4\beta_1^7}{\Gamma_1^7} + (p+2)\frac{\mu_2^4\beta_2^7}{\Gamma_2^7}\right)\,, \tag{100}$$

$$\mathcal{O}_4 = \frac{3}{2} J_2 R^2 \left(-p \frac{\mu_1^4 \beta_1^7}{\Gamma_1^7} + (p+3) \frac{\mu_2^4 \beta_2^7}{\Gamma_2^7} \right), \tag{101}$$

$$\mathcal{S}_1 = \frac{\mathcal{G}\mu_2 m_1 m_2 \beta_2^2}{\Gamma_2^3} \left(\frac{\mu_2 \beta_2^2}{\mu_1 \beta_1^2} \left[\left(1 + \frac{p}{2} \right) \frac{\Gamma_1^2}{\Gamma_2^2} + \frac{p}{2} \frac{\Gamma_1}{\Gamma_2} \right] D + 1 + \frac{p}{2} \right) b_{\frac{1}{2}}^{(0)}(\alpha_0), \tag{102}$$

$$\mathcal{S}_2 = -\frac{\mathcal{G}\mu_2 m_1 m_2 \beta_2^2}{2\Gamma_1 \Gamma_2^2} \left[\alpha_0 D + \frac{1}{2} \alpha_0^2 D^2 \right] b_{\frac{1}{2}}^{(0)}(\alpha_0), \tag{103}$$

$$\mathcal{S}_3 = -\frac{\mathcal{G}\mu_2 m_1 m_2 \beta_2^2}{2\Gamma_2^3} \left[\alpha_0 D + \frac{1}{2} \alpha_0^2 D^2 \right] b_{\frac{1}{2}}^{(0)}(\alpha_0), \tag{104}$$

$$\mathcal{S}_4 = -\frac{\mathcal{G}\mu_2 m_1 m_2 \beta_2^2}{2\Gamma_2^2 \sqrt{\Gamma_1 \Gamma_2}} \left[2 - 2\alpha_0 D - \alpha_0^2 D^2 \right] b_{\frac{1}{2}}^{(1)}(\alpha_0), \tag{105}$$

$$\mathcal{S}_5 = \frac{\mathcal{G}\mu_2 m_1 m_2 \beta_2^2}{4\Gamma_1 \Gamma_2^2} \alpha_0 b_{\frac{3}{2}}^{(1)}(\alpha_0), \tag{106}$$

$$\mathcal{S}_6 = \frac{\mathcal{G}\mu_2 m_1 m_2 \beta_2^2}{4\Gamma_2^3} \alpha_0 b_{\frac{3}{2}}^{(1)}(\alpha_0), \tag{107}$$

$$\mathcal{S}_7 = -\frac{\mathcal{G}\mu_2 m_1 m_2 \beta_2^2}{2\Gamma_2^2 \sqrt{\Gamma_1 \Gamma_2}} \alpha_0 b_{\frac{3}{2}}^{(1)}(\alpha_0), \tag{108}$$

$$\mathcal{R}_1 = -\frac{\mathcal{G}\mu_2 m_1 m_2 \beta_2^2}{2\Gamma_1 \Gamma_2^2} \left(\frac{8p^2 + 11pq + 3q^2}{q^2} + \frac{4p + 3q}{q} \alpha_0 D + \frac{\alpha_0^2}{2} D^2 \right) b_{\frac{1}{2}}^{(p+2)}(\alpha_0), \tag{109}$$

$$\mathcal{R}_2 = -\frac{\mathcal{G}\mu_2 m_1 m_2 \beta_2^2}{2\Gamma_2^3} \left(\frac{8p^2 + 9pq + 2q^2}{q^2} + \frac{4p + 3q}{q} \alpha_0 D + \frac{\alpha_0^2}{2} D^2 \right) b_{\frac{1}{2}}^{(p)}(\alpha_0) + \mathcal{R}_2^*, \tag{110}$$

where

$$\mathcal{R}_2^* = \begin{cases} \frac{9}{4} \frac{\beta_1 \beta_2 \mu_1 \mu_2}{\Gamma_1 \Gamma_2^2} & \text{if} \quad p = 1 \\ 0 & \text{if} \quad p \neq 1 \end{cases}, \tag{111}$$

$$\mathcal{R}_3 = -\frac{\mathcal{G}\mu_2 m_1 m_2 \beta_2^2}{\Gamma_2^2\sqrt{\Gamma_1\Gamma_2}}\left(\frac{8p^2+10pq+3q^2}{q^2}+\frac{4p+3q}{q}\alpha_0 D + \frac{\alpha_0^2}{2}D^2\right) b_{\frac{1}{2}}^{(p+1)}(\alpha_0)\,, \tag{112}$$

$$\mathcal{R}_4 = -\frac{\mathcal{G}\mu_2 m_1 m_2 \beta_2^2}{4\Gamma_1\Gamma_2^2}\alpha_0 b_{\frac{3}{2}}^{(p+1)}(\alpha_0)\,, \tag{113}$$

$$\mathcal{R}_5 = -\frac{\mathcal{G}\mu_2 m_1 m_2 \beta_2^2}{4\Gamma_2^3}\alpha_0 b_{\frac{3}{2}}^{(p+1)}(\alpha_0)\,, \tag{114}$$

$$\mathcal{R}_6 = \frac{\mathcal{G}\mu_2 m_1 m_2 \beta_2^2}{2\Gamma_2^2\sqrt{\Gamma_1\Gamma_2}}\alpha_0 b_{\frac{3}{2}}^{(p+1)}(\alpha_0)\,, \tag{115}$$

where $D = \frac{\partial}{\partial\alpha_0}$ and $\alpha_0 = 0.7114$ is equal to $\alpha = a_1/a_2$ at nominal resonance (Eq.64).

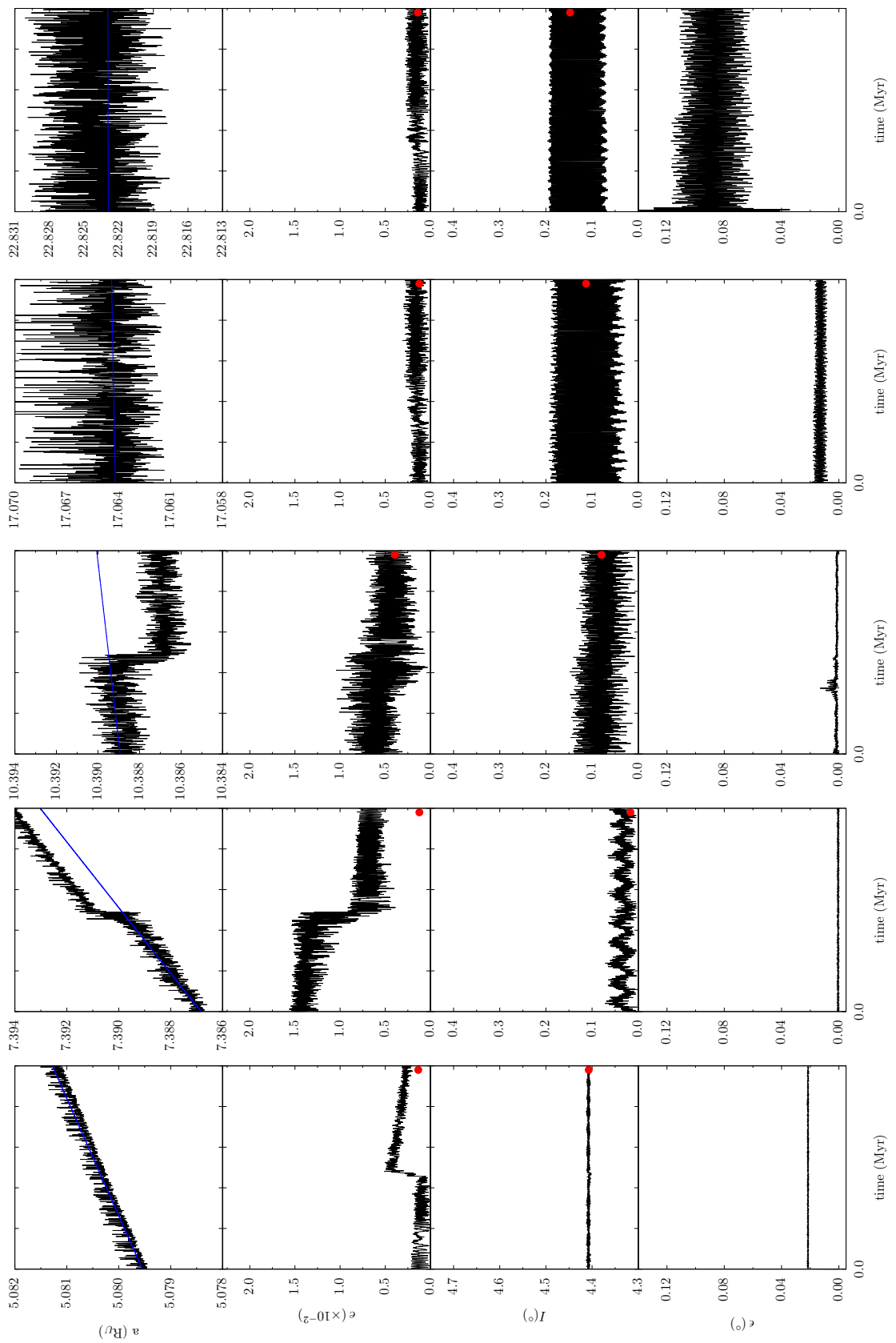

Figure 14: Simulation with the five-satellite model for the passage through the 5/3 MMR between Ariel and Umbriel. From the top to the bottom, we show the semi-major axes, the eccentricities, the inclinations, and the obliquities. The system evolves from initial $e_1 = 0.015$, $e_2 = 0.005$, $I_1 = 0.001°$, and $I_2 = 0.082°$. The initial eccentricities and inclinations of Miranda, Titania, and Oberon correspond to their current mean values (Table 1). The asymptotic tidal evolution of the semi-major axis (see Sect. 3.1 in Paper I) is represented with a blue line, and the present mean eccentricities and inclinations are marked with red dots.

B. Complete secular dynamics: escape probabilities

Table 5: Escape probability from the 5/3 Ariel-Umbriel MMR for a mesh of 625 initial (e_1, e_2, I_1, I_2). Each set encompass a total 1 000 runs equally distributed over the resonance angle σ (Eq. (13)).

		$e_2 = 1\times10^{-5}$					$e_2 = 5\times10^{-3}$					$e_2 = 1\times10^{-2}$					$e_2 = 1.5\times10^{-2}$					$e_2 = 2\times10^{-2}$				
	I_2 (°) / I_1 (°)	0.001	0.05	0.10	0.15	0.20	0.001	0.05	0.10	0.15	0.20	0.001	0.05	0.10	0.15	0.20	0.001	0.05	0.10	0.15	0.20	0.001	0.05	0.10	0.15	0.20
$e_1 = 1\times10^{-5}$	0.001	0.0	0.0	0.0	0.0	0.0	0.0	0.0	0.0	0.0	0.0	5.4	4.6	4.2	5.2	5.2	9.8	13.9	13.2	15.0	14.2	5.8	11.8	13.4	15.8	14.9
	0.05	0.0	0.0	0.0	0.0	0.0	0.0	0.0	0.0	0.0	0.0	6.2	4.8	4.7	4.5	4.8	13.9	14.1	15.7	16.2	14.2	13.9	14.3	13.2	14.4	15.2
	0.10	0.0	0.0	0.0	0.0	0.0	0.0	0.0	0.0	0.0	0.0	5.8	5.6	5.5	5.9	5.7	15.8	14.2	14.2	15.3	12.9	12.8	15.6	15.4	16.0	14.6
	0.15	0.0	0.0	0.0	0.0	0.0	0.0	0.0	0.0	0.0	0.0	4.8	4.8	5.7	5.6	5.1	13.9	15.6	16.7	13.3	13.5	16.1	16.0	14.3	15.1	17.5
	0.20	0.0	0.0	0.0	0.0	0.0	0.0	0.0	0.0	0.0	0.0	5.3	5.2	5.0	4.2	4.6	14.0	15.0	14.4	13.3	14.9	16.1	17.1	16.9	13.8	17.2
$e_1 = 5\times10^{-3}$	0.001	0.0	0.0	0.0	0.0	0.0	0.0	0.0	0.0	0.0	0.0	13.0	10.7	10.3	11.7	10.8	10.3	14.3	16.8	13.5	15.4	4.5	12.7	13.2	13.3	12.0
	0.05	0.0	0.0	0.0	0.0	0.0	0.0	0.0	0.0	0.0	0.0	11.9	10.3	11.6	11.3	8.5	16.5	17.6	16.2	15.6	14.7	9.8	11.5	11.9	12.3	13.0
	0.10	0.0	0.0	0.0	0.0	0.0	0.0	0.0	0.0	0.1	0.0	11.0	13.2	12.4	12.5	10.9	14.0	15.2	16.6	16.6	15.5	12.9	12.8	11.9	12.4	13.5
	0.15	0.0	0.0	0.0	0.0	0.0	0.0	0.0	0.0	0.0	0.1	11.3	11.1	11.6	10.4	9.6	17.6	15.4	15.1	15.5	16.7	11.7	14.6	14.5	12.4	14.4
	0.20	0.0	0.0	0.0	0.0	0.0	0.0	0.0	0.0	0.2	0.0	10.2	11.6	11.3	11.4	10.7	15.9	15.0	14.4	15.5	14.5	13.0	14.0	12.8	13.5	13.8
$e_1 = 1\times10^{-2}$	0.001	21.9	20.9	18.7	17.6	20.2	38.5	36.5	33.3	33.6	31.9	23.3	32.8	34.4	36.6	34.5	12.1	19.5	20.5	26.3	22.4	6.2	9.6	12.4	12.9	14.1
	0.05	19.0	20.8	19.7	18.3	17.5	31.1	32.2	32.7	32.0	29.1	33.5	33.5	34.3	36.3	34.2	22.8	23.4	21.4	25.8	25.7	11.3	12.2	12.7	10.3	14.7
	0.10	18.0	22.5	19.2	20.2	15.3	30.0	33.8	34.1	34.5	31.1	36.3	34.7	33.9	36.3	32.7	23.3	22.6	23.8	25.6	25.1	12.4	14.1	13.6	14.6	12.4
	0.15	14.8	18.7	18.4	18.0	13.4	30.4	32.0	31.9	32.1	26.6	33.5	35.7	35.6	33.0	32.4	24.9	26.4	25.8	27.3	24.6	18.6	14.8	16.0	15.2	15.2
	0.20	10.6	11.3	13.3	12.4	13.6	26.9	26.9	25.2	26.3	24.8	33.1	35.6	30.1	34.9	30.3	25.6	25.5	24.3	27.3	26.6	15.3	17.4	17.4	17.1	14.5
$e_1 = 1.5\times10^{-2}$	0.001	48.7	54.8	61.1	63.3	58.8	58.5	67.3	69.3	68.3	71.7	37.2	42.3	45.0	49.7	47.7	24.6	25.4	25.6	26.4	28.9	15.5	15.6	16.0	17.7	19.1
	0.05	61.7	62.8	63.1	62.4	61.6	68.8	69.3	68.4	70.4	69.0	43.3	42.9	44.6	48.6	49.9	25.6	23.7	25.3	24.1	29.1	15.8	16.4	16.0	17.7	17.3
	0.10	60.7	59.3	58.8	59.3	59.1	68.1	68.2	68.8	67.7	64.9	49.3	49.6	51.3	46.7	51.4	25.4	26.7	28.9	31.2	29.2	16.8	17.1	17.9	17.4	16.2
	0.15	58.8	57.9	55.5	55.3	55.1	63.5	61.3	63.1	63.6	61.1	50.5	50.8	49.6	50.6	53.5	29.6	32.6	37.8	29.4	29.7	17.2	19.1	17.3	19.5	17.2
	0.20	50.9	53.8	52.7	48.6	51.4	60.9	58.4	59.3	55.8	57.1	50.5	49.6	51.1	50.9	51.0	32.5	31.3	29.2	30.4	33.1	19.7	20.4	21.0	18.2	19.4
$e_1 = 2\times10^{-2}$	0.001	60.4	66.1	72.0	74.4	73.9	74.0	74.9	77.3	77.7	79.4	44.1	48.5	47.8	52.7	53.2	36.0	40.0	35.9	36.7	36.4	24.7	24.5	24.5	24.8	24.5
	0.05	68.8	68.3	68.5	76.2	77.4	77.7	79.0	78.7	79.1	80.2	50.0	48.6	58.8	49.4	51.4	39.4	36.9	37.9	40.0	36.3	25.5	25.0	26.6	25.8	25.9
	0.10	76.7	76.2	75.7	78.3	76.6	81.5	78.5	82.1	78.9	80.5	52.2	47.8	51.0	49.7	51.9	39.7	39.3	40.4	40.9	37.0	27.1	23.8	27.6	23.0	26.6
	0.15	77.8	75.3	75.3	75.0	73.1	78.8	80.3	80.2	77.5	81.0	50.6	55.7	52.9	54.7	54.8	38.0	38.6	38.5	42.7	39.0	24.7	25.9	23.7	27.0	24.0
	0.20	74.8	73.5	73.9	70.7	71.1	75.4	75.0	79.1	76.9	76.4	57.0	58.5	55.0	53.3	52.4	37.2	39.3	38.6	38.5	38.8	24.0	24.9	25.9	24.5	25.9